

# Dwarf AGNs from Variability for the Origins of Seeds (DAVOS): Intermediate-mass black hole demographics from optical synoptic surveys

Colin J. Burke,<sup>1,2</sup>★ Yue Shen,<sup>1,3</sup> Xin Liu,<sup>1,3</sup> Priyamvada Natarajan,<sup>4,5</sup> Neven Caplar,<sup>6</sup> Jillian M. Bellovary<sup>7,8,9</sup> and Z. Franklin Wang<sup>1</sup>

<sup>1</sup>Department of Astronomy, University of Illinois at Urbana-Champaign, 1002 W. Green Street, Urbana, IL 61801, USA

<sup>2</sup>Center for AstroPhysical Surveys, National Center for Supercomputing Applications, 1205 W. Clark Street, Urbana, IL 61801, USA

<sup>3</sup>National Center for Supercomputing Applications, 1205 W. Clark Street, Urbana, IL 61801, USA

<sup>4</sup>Department of Astronomy, Yale University, 260 Whitney Avenue, New Haven, CT 06511, USA

<sup>5</sup>Black Hole Initiative, Harvard University, 20 Garden Street, Cambridge, MA 02138, USA

<sup>6</sup>Department of Astrophysical Sciences, Princeton University, 4 Ivy Lane, 08544, Princeton, NJ, USA

<sup>7</sup>Department of Physics, Queensborough Community College, City University of New York, 222-05 56th Ave, Bayside, NY, 11364, USA

<sup>8</sup>Department of Astrophysics, American Museum of Natural History, Central Park West at 79th Street, New York, NY 10024, USA

<sup>9</sup>Department of Physics, Graduate Center, City University of New York, New York, NY 10016, USA

Accepted XXX. Received YYY; in original form ZZZ

## ABSTRACT

We present a phenomenological forward Monte Carlo model for forecasting the population of active galactic nuclei (AGNs) in dwarf galaxies observable via their optical variability. Our model accounts for expected changes in the spectral energy distribution of AGNs in the intermediate-mass black hole (IMBH) mass range and uses observational constraints on optical variability as a function of black hole (BH) mass to generate mock light curves. Adopting several different models for the BH occupation function, including one for off-nuclear IMBHs, we quantify differences in the predicted local AGN mass and luminosity functions in dwarf galaxies. As a result, we are able to model the variable fraction of AGNs as a function of physical host properties, such as host galaxy stellar mass, in the presence of selection effects. We find that our adopted occupation fractions for the “heavy” and “light” initial BH seeding scenarios can be distinguished with variability at the  $2 - 3\sigma$  level for galaxy host stellar masses below  $\sim 10^8 M_\odot$  with the Vera C. Rubin Observatory. We demonstrate the prevalence of a selection bias whereby recovered IMBH masses fall, on average, above the predicted value from the local host galaxy - BH mass scaling relation with the strength of the bias dependent on the survey sensitivity. Our methodology can be used more broadly to calibrate AGN demographic studies in synoptic surveys. Finally, we show that a targeted  $\sim$  hourly cadence program over a few nights with the Rubin Observatory can provide strong constraints on IMBH masses given their expected rapid variability timescales.

**Key words:** (galaxies:) dwarf, nuclei, quasars: supermassive black holes – black hole physics

## 1 INTRODUCTION

Understanding the population of active galactic nuclei (AGN) in the local Universe can provide insights into the growth and evolution of supermassive black holes (SMBHs) across cosmic time. While virtually every massive galaxy contains a SMBH in its center, the occupation fraction of black holes in the dwarf galaxy regime remains poorly constrained. There is strong evidence for the existence of  $\sim 10^5 - 10^6 M_\odot$  black holes in dwarf galaxies (Filippenko & Ho 2003; Barth et al. 2004; Reines & Volonteri 2015; Baldassare et al. 2015). However, with the exception of the recent gravitational wave event GW190521 with a merger remnant mass of  $142^{+28}_{-16} M_\odot$  (LIGO Scientific Collaboration & Virgo Collaboration 2020), the X-ray tidal disruption event 3XMM J215022.4-055108 (Lin et al. 2018), and the somewhat more controversial  $M_{\text{BH}} \sim 10^4 M_\odot$  hyper-luminous X-ray source ESO 243-49 HLX-1 (Farrell et al. 2009), intermediate-mass

black holes (IMBHs) with  $M_{\text{BH}} \sim 10^2 - 10^4 M_\odot$  remain difficult to identify (Greene et al. 2020).

To explain these observations, as well as the formation of SMBHs at high redshifts when the Universe was only a few hundred Myr old (e.g., Fan et al. 2001; Wu et al. 2015; Bañados et al. 2018; Wang et al. 2021), it is thought that SMBHs must grow via accretion and mergers from early seed black holes (e.g., Natarajan 2014; Inayoshi et al. 2020). Theories of SMBH seeding scenarios broadly fall into two classes: “light” and “heavy” seeds. In the most popular light seed scenario, black holes with masses of  $\sim 10^{1-2} M_\odot$  are expected to form as remnants of the massive, first generation of stars, namely the Population III (Pop III) stars (Bond et al. 1984; Madau & Rees 2001; Fryer et al. 2001; Abel et al. 2002; Bromm & Loeb 2003). With improvement in the resolution of simulations that track the formation of first stars, it is now found that rather than forming individual stars, early star formation results in star clusters, whose evolution could also provide sites for the formation of light initial seeds (Gürkan et al. 2004; Portegies Zwart et al. 2004). On the other hand, in the most popular “heavy” seed scenario, black holes with masses

★ E-mail: colinjb2@illinois.edu (CJB)

of  $\sim 10^4 - 10^6 M_{\odot}$  are expected to viably form from direct collapse of primordial gas clouds under specific conditions (Haehnelt & Rees 1993; Loeb & Rasio 1994; Bromm & Loeb 2003; Koushiappas et al. 2004; Lodato & Natarajan 2006; Begelman et al. 2006; Lodato & Natarajan 2007). Additionally multiple other formation channels have also been proposed, such as mechanisms within nuclear star clusters (Devecchi & Volonteri 2009; Davies et al. 2011; Devecchi et al. 2010; Alexander & Natarajan 2014; Lupi et al. 2014; Antonini et al. 2015; Stone et al. 2017; Fragione & Silk 2020; Kroupa et al. 2020; Natarajan 2021); inside globular clusters (Miller & Hamilton 2002; Leigh et al. 2014; Antonini et al. 2019), and even young star clusters (Rizzuto et al. 2021). Heavy seeds are predicted to be fewer in number, while light seeds are predicted to be more common but less massive (Lodato & Natarajan 2007). Given that the host galaxy stellar mass and mass of the inactive and active central black holes (BHs) appear to be correlated at least in the local Universe; Magorrian et al. 1998; Reines & Volonteri 2015), the occupation fraction (i.e., fraction of galaxies containing a central BH at a given stellar mass) is expected be an observational tracer of seeding (Volonteri et al. 2008; Greene 2012). Counter-intuitively, despite their complex growth history via accretion and mergers, the local occupation fraction in the dwarf galaxy mass range ( $M_{\star} \lesssim 10^{9.5} M_{\odot}$ ) is predicted to be particularly sensitive to early seeding physics (but see Mezcua (2019)). Even at these late cosmic times and on these small dwarf galaxy scales, estimates of the occupation fraction might permit discriminating between the light and heavy seeding scenarios (Volonteri et al. 2008).

Deep X-ray surveys have been used to identify low-mass and low-luminosity AGNs at low and intermediate redshifts (Fiore et al. 2012; Young et al. 2012; Civano et al. 2012; Miller et al. 2015; Mezcua et al. 2016; Luo et al. 2017; Xue 2017). However, these surveys are expensive and are often plagued by contamination from X-ray binaries. Radio searches have also successfully identified low-mass AGNs in as radio cores in star-forming dwarf galaxies (Mezcua et al. 2019; Reines et al. 2020), although they are subject to the low detection rates. Traditional AGN search techniques at optical wavelengths, such as narrow-emission line diagnostics (Baldwin et al. 1981; Veilleux & Osterbrock 1987), on the other hand tend to miss a large fraction of IMBHs preferentially in star-forming (Baldassare et al. 2016; Trump et al. 2015; Agostino & Salim 2019) and low-metallicity (Groves et al. 2006) host galaxies. However, systematic searches using wide-area optical surveys have begun to uncover this previously-hidden population of accreting black holes in dwarf galaxies. One popular technique that has been pursued is the mining of large databases of optical spectra for broad emission features in Balmer emission lines (Greene & Ho 2007; Chilingarian et al. 2018; Liu et al. 2018). However, this method requires high  $S/N$  spectra to detect the very low-luminosity broad emission (Burke et al. 2021c). In addition, it suffers from contamination from supernovae and stellar winds, which can both produce transient broad Balmer emission with luminosities identical to a dwarf AGN. Confirmation of the detection of dwarf AGN further requires multi-epoch spectroscopy to ensure the broad emission is persistent (Baldassare et al. 2016). Finally, it has been suggested that some accreting IMBHs may fail to produce a broad line region at all (Chakravorty et al. 2014).

The possibility that some IMBHs live outside their host galaxy nuclei—the so called “wandering” BH population—is another complicating factor for systematic searches of IMBHs (Volonteri & Perna 2005; Bellovary et al. 2010; Mezcua et al. 2015; Mezcua & Domínguez Sánchez 2020; Bellovary et al. 2019; Reines et al. 2020; Ricarte et al. 2021a,b; Ma et al. 2021). As recently demonstrated from the analysis of the Romulus suite of simulations (Ricarte et al. 2021a)

demonstrate that a variety of dynamical mechanisms could result in a population of wandering IMBHs in galaxies, such as tidal stripping of merging dwarf galaxies (Zinnecker et al. 1988); gravitational recoil from galaxy centers (Volonteri et al. 2003; Holley-Bockelmann et al. 2008; O’Leary & Loeb 2009; Blecha et al. 2011, 2016), or gravitational runaway processes in star clusters (Miller & Hamilton 2002; Portegies Zwart & McMillan 2002; Fragione et al. 2018).

Recently, searches for optical variability in wide-area optical surveys have uncovered hundreds of dwarf AGN candidates (Baldassare et al. 2018, 2020; Burke et al. 2021a; Martínez-Palomera et al. 2020; Ward et al. 2021). These sources have enabled studies that have improved our understanding of AGN optical variability across a vast range of mass scales. Variability is thought to be driven by the inner UV-emitting regions of their rapidly-accreting accretion disks (Burke et al. 2021b). In this work, we leverage these recent advances in IMBH identification and optical variability behavior, along with extrapolations of known host-galaxy correlations observed in the low-mass regime (e.g., Reines & Volonteri 2015), to forecast the IMBH population that could be detectable by upcoming time-domain imaging surveys.

This work is organized as follows. In §2, we develop a forward model to forecast the number density of IMBHs in dwarf galaxies. In §3, we adapt this model to generate simulated observations mimicking light curves expected from the Vera C. Rubin Observatory Legacy Survey of Space and Time (LSST Rubin; Ivezić et al. 2019) and the Palomar Transient Factory (PTF) survey (Law et al. 2009) to compare with existing observations (Baldassare et al. 2020). We opt for the PTF comparison over a similar study with SDSS (Baldassare et al. 2018) because the PTF study has a larger sample size which enables tighter constraints on the variable fraction while being broadly consistent with the SDSS data. A comparison with the Dark Energy Survey is presented separately in Burke et al. (2021a). We demonstrate the capability of our model to reproduce the IMBH detection fraction as a function of stellar mass consistent with existing AGN demographic studies. A concordance  $\Lambda$ CDM cosmology with  $\Omega_m = 0.3$ ,  $\Omega_{\Lambda} = 0.7$ , and  $H_0 = 70 \text{ km s}^{-1} \text{ Mpc}^{-1}$  is assumed throughout. Unless stated otherwise, all uncertainty bands in the figures are  $1\sigma$ , estimated using the 16th and 84th percentiles of the probability density distributions, and points are the distribution means. Duplicate symbols are used for some parameters throughout this work. The reader should refer to the context to resolve any ambiguity.

## 2 METHODOLOGY TO CONSTRUCT THE DEMOGRAPHIC MODEL

Broadly following the basic methodology presented in prior work by Caplar et al. (2015) and Weigel et al. (2017), we develop an empirically motivated forward model starting from the galaxy stellar mass function and host-galaxy scaling relations to derive the corresponding BH mass and AGN luminosity functions (also see Gallo & Sesana 2019; Greene et al. 2020). Our goal is to estimate the number density of dwarfs with central AGNs in the IMBH mass range that would result from the various proposed seeding mechanisms. Therefore, we must extrapolate scaling relations derived from current observational constraints on the galaxy population from host galaxy correlations as well as the Eddington ratio distribution derived for more massive AGNs to lower mass BHs. A summary table of parameters and our adopted values for them are provided in Table 1, unless otherwise explicitly quoted in the text.

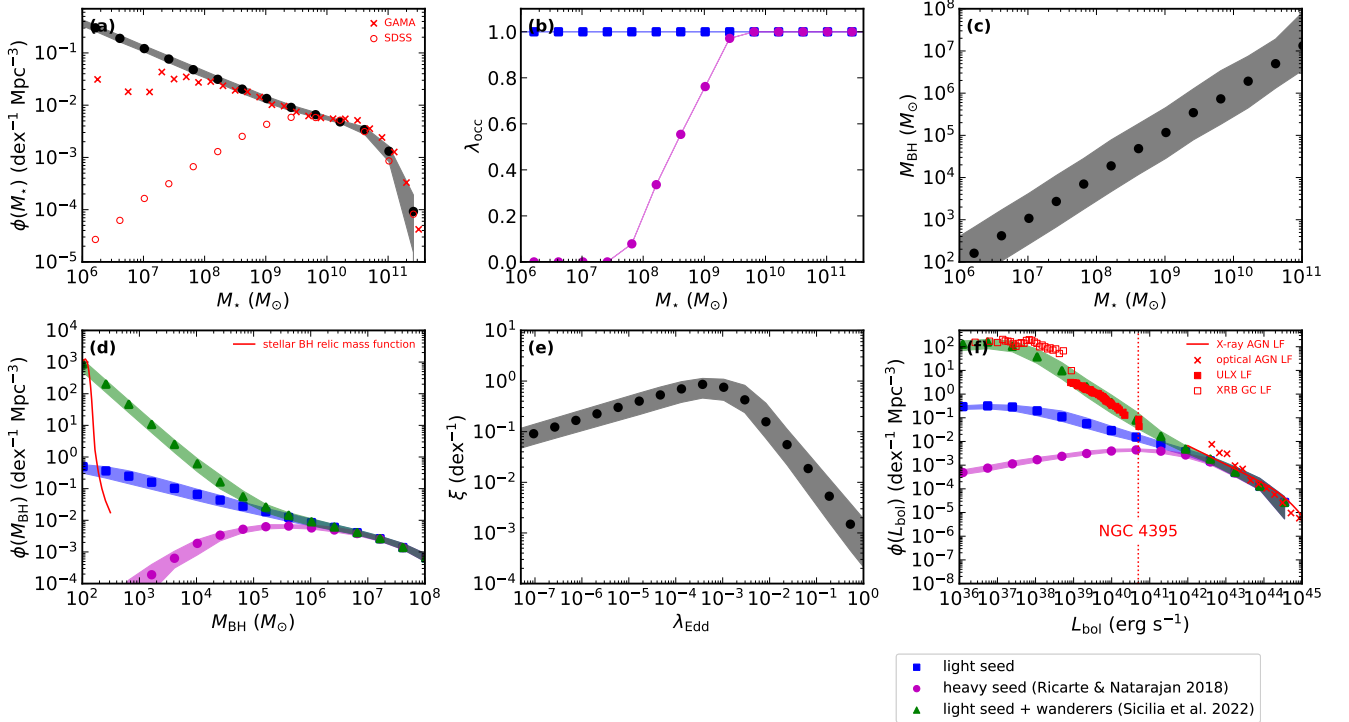


**Figure 1.** Monte Carlo model for local AGN demographics in dwarf galaxies. We start from the galaxy stellar mass function (a) and consider two possibilities for the occupation fraction (a ‘light’ seed scenario in blue/square symbols and a ‘heavy’ seed scenario in magenta/circle symbols; b). Then, we use the local  $M_{\text{BH}} - M_{\star}$  scaling relation to predict the BH mass function (d). Finally, we assume a power-law distribution for the Eddington ratios (e) to predict the local bolometric AGN luminosity function (LF) (f). The shaded bands are  $1\sigma$  uncertainties, estimated using the 16th and 84th percentiles of the distributions, and points are the distribution means. The red ‘x’ symbols are the observational constraints on the local galaxy stellar mass function (points below  $\sim 10^8 M_{\odot}$ ) are effected by incompleteness of low surface brightness galaxies; Baldry et al. 2012 (a) and the local AGN luminosity function from optical observations (Schulze et al. 2009; Hao et al. 2005) (f). The red curve in panel (d) is stellar BH relic mass function anchored to merger rates from gravitational wave observations (Sicilia et al. 2022). The red ‘o’ symbols is the GSMF measured from the SDSS-based NASA Sloan Atlas catalog (Blanton et al. 2011), which demonstrates the spectroscopic incompleteness at low stellar mass (a). The red filled squares in panel (f) is the observed luminosity function of ultra-luminous X-ray sources derived from seven collisional ring galaxies (Wolter et al. 2018) normalized to the number density of  $M_{\star} \sim 10^6 M_{\odot}$  dwarf galaxies after excluding sources with  $L_{0.5-10 \text{ keV}} < 10^{39} \text{ erg s}^{-1}$  where the sample is incomplete. The red open squares in panel (f) is the observed luminosity function of X-ray binaries (XRBs) in globular clusters (GCs) in nearby galaxies (Lehmer et al. 2020) normalized to the number density of  $M_{\star} \sim 10^6 M_{\odot}$  dwarf galaxies. The red dotted vertical line in panel (f) represents the bolometric luminosity of the  $M_{\text{BH}} \sim 10^4 - 10^5 M_{\odot}$  dwarf Seyfert galaxy NGC 4395 (Filippenko & Ho 2003; Moran et al. 1999).

## 2.1 The dwarf galaxy population

We begin by considering the number density of galaxies in the local Universe. At a given redshift, the measured galaxy stellar mass function (GSMF) is well-described by a double power-law function of the form,

$$\phi(M_{\star}) dM_{\star} = e^{-M_{\star}/M_{\star}^*} \left[ \phi_1 \left( \frac{M_{\star}}{M_{\star}^*} \right)^{\alpha_1} + \phi_2 \left( \frac{M_{\star}}{M_{\star}^*} \right)^{\alpha_2} \right] \frac{dM_{\star}}{M_{\star}^*}, \quad (1)$$

where  $\phi = dn_{\star}/dM_{\star}$ ,  $M_{\star}$  is the galaxy stellar mass,  $n_{\star}$  is the number density,  $M_{\star}^*$  is the break stellar mass,  $\alpha_1$  and  $\alpha_2$  are the shallow and steep power law exponents, respectively, and  $\phi_1$  and  $\phi_2$  are normalization factors that correspond to the low and high mass end of the GSMF, respectively (Schechter 1976). We adopt the best-fit parameters from Wright et al. (2017) based on the Galaxy And Mass Assembly (GAMA) low-redshift  $\sim 180 \text{ deg}^2$  spectroscopic survey, which has a spectroscopic depth of  $r \sim 19.8 \text{ mag}$  (Driver et al. 2011; Liske et al. 2015). The GAMA survey measured GSMF is good to  $z \sim 0.1$  and for  $M_{\star} \gtrsim 10^{7.5} M_{\odot}$  but is also consistent with current limits on the GSMF down to  $M_{\star} \sim 10^{6.5} M_{\odot}$  from deep G10-COSMOS imaging—a  $\sim 1 \text{ deg}^2$  subset of the GAMA survey

overlapping with the Cosmic Evolution Survey (Scoville et al. 2007) with a spectroscopic depth of  $r \sim 24.5 \text{ mag}$  (Andrews et al. 2017).

The high mass end of the GSMF is mostly constituted by red galaxies, while the low mass end of the GSMF is dominated by blue galaxies. Although the Wright et al. (2017) parameters are well-constrained for the low-mass end of the GSMF, they do not include separate derived GSMFs and tailored fits for the red and blue galaxy populations. Therefore, we use the ratio of the GSMFs partitioned between the red and blue galaxy populations from Baldry et al. (2012), which is consistent with the results of Wright et al. (2017), to separately populate red and blue galaxies in our model. We assign each galaxy a ‘red’ or ‘blue’ identifier, which we use to determine the accretion mode, that differs between these two galaxy populations (Weigel et al. 2017; Ananna et al. 2022). We ignore any redshift dependence in the GSMF, as we show that the number of detectable IMBHs drops off quickly with redshift at the expected sensitivities ( $g \sim 25 \text{ mag}$ ) for LSST Rubin currently being considered. Our LSST model-predicted, detectable IMBHs are expected to mostly lie at  $z \lesssim 0.05$ .

The number of random draws  $N_{\text{draw}}$  can be defined in terms of the

**Table 1.** Table of parameters, our adopted values and their  $1\sigma$  uncertainties describing the galaxy population of our Monte Carlo model.

Parameter	Value	Unit	Reference
Galaxy Stellar Mass Function (GSMF)			
$\log(M_\star^*/M_\odot)$	$10.78 \pm 0.01$	dex	<a href="#">Wright et al. (2017)</a>
$\phi_1/10^{-3}$	$2.93 \pm 0.40$	$\text{Mpc}^{-3}$	...
$\phi_2/10^{-3}$	$0.63 \pm 0.10$	$\text{Mpc}^{-3}$	...
$\alpha_1$	$-0.62 \pm 0.03$		...
$\alpha_2$	$-1.50 \pm 0.01$		...
<sup>a,b</sup> Blue+Green Galaxy Stellar Mass Function (GSMF)			
$\log(M_\star^*/M_\odot)$	10.72	$\text{Mpc}^{-3}$	<a href="#">Baldry et al. (2012)</a>
$\phi/10^{-3}$	0.71		...
$\alpha$	-1.45		...
<sup>a</sup> Red Galaxy Stellar Mass Function (GSMF)			
$\log(M_\star^*/M_\odot)$	10.72	dex	<a href="#">Baldry et al. (2012)</a>
$\phi_1/10^{-3}$	3.25	$\text{Mpc}^{-3}$	...
$\phi_2/10^{-3}$	0.08	$\text{Mpc}^{-3}$	...
$\alpha_1$	-0.45		...
$\alpha_2$	-1.45		...
<sup>c</sup> Host Galaxy-Black Hole Mass Scaling			
$\log(M_\star^*/M_\odot)$	11	dex	<a href="#">Reines &amp; Volonteri (2015)</a>
$\alpha$	$7.45 \pm 0.08$		...
$\beta$	$1.05 \pm 0.11$		...
Blue+Green Eddington Ratio Distribution Function (ERDF)			
$\log(\lambda_{\text{Edd}}^*)$	$-1.84^{+0.30}_{-0.37}$		<a href="#">Weigel et al. (2017)</a>
$\delta_1$	-0.2		<sup>d</sup>
$\delta_2$	$2.53^{+0.68}_{-0.38}$		<a href="#">Weigel et al. (2017)</a>
$\log(\lambda_{\text{Edd,min}})$	-8		
$\log(\lambda_{\text{Edd,max}})$	0		
Red Eddington Ratio Distribution Function (ERDF)			
$\log(\lambda_{\text{Edd}}^*)$	$-2.84^{+0.22}_{-0.14}$		<a href="#">Weigel et al. (2017)</a>
$\delta_1$	-0.3		<sup>d</sup>
$\delta_2$	$1.22^{+0.19}_{-0.13}$		<a href="#">Weigel et al. (2017)</a>
$\log(\lambda_{\text{Edd,min}})$	-8		
$\log(\lambda_{\text{Edd,max}})$	0		

<sup>a</sup> We use the [Wright et al. \(2017\)](#) GSMF, which is better-constrained in the dwarf galaxy regime, but use the separate blue+green and red GSMFs from [Baldry et al. \(2012\)](#) to determine the relative ratio of the blue+green and red galaxy populations (see text for details).

<sup>b</sup> This is a single [Schechter \(1976\)](#) function in [Baldry et al. \(2012\)](#).

<sup>c</sup> We adopt the rms scatter in the relation of  $\sim 0.55$  dex in the  $M_\star$  direction ([Reines & Volonteri 2015](#)).

<sup>d</sup> We re-normalized the  $\delta_1$  parameters to better approximate the variable fraction of the entire galaxy population. Our normalization is still consistent with the local AGN luminosity function.

GSMF and the survey volume as:

$$N_{\text{draw}} = V(z_{\text{min}}, z_{\text{max}}, \Omega) \int_{M_{\star,\text{min}}}^{M_{\star,\text{max}}} \phi(M_\star) dM_\star, \quad (2)$$

where  $V$  is comoving volume between redshifts  $z_{\text{min}}$  and  $z_{\text{max}}$  over solid angle  $\Omega$ . With each draw we randomly assign  $N_{\text{draw}}$  galaxies a stellar mass using Equation 1 as the target distribution with  $z_{\text{min}} = 0$ ,  $z_{\text{max}} = 0.055$ . Our choice of  $z_{\text{max}} = 0.055$  is chosen to match existing observational constraints ([Baldassare et al. 2020](#)), and we show that the number of detectable IMBHs falls off dramatically

with increasing redshift. This assumption of the restriction of the redshift range under scrutiny assumption also allows us to ignore any explicit redshift dependence in the GSMF. The galaxy redshifts are determined by randomly assigning each galaxy to a redshift bin out to  $z_{\text{max}}$ , where the number of galaxies in each redshift bin is then proportional to the cosmological differential comoving volume at that redshift bin. As a consistency check, we show that the redshift and stellar mass distributions of our mock sample compare extremely well to observed SDSS galaxies in Appendix A.

## 2.2 Occupation fraction

After determining  $N_{\text{draw}}$ , we then consider different possible functional forms for the occupation fraction, the fraction of galaxies hosting an IMBH/SMBH,  $\lambda_{\text{occ}}(M_\star)$ . We refer to this quantity as the *occupation function*. This quantity may be greater than unity if multiple IMBHs are harbored in a galaxy. We explore the following scenarios for the occupation function:

(i) **Light seeds:** A constant occupation function of  $\lambda_{\text{occ}} = 1$  shown in blue in Figure 1. This represents the most optimistic predictions for an initial “light” seed scenario (e.g., from Pop. III stellar remnants) as examined in [Ricarte & Natarajan \(2018\)](#).

(ii) **Heavy seeds:** An occupation function that approaches unity for massive galaxies ( $M_\star > 10^9 M_\odot$ ) but drops dramatically by  $M_\star \sim 10^8 M_\odot$ , shown in magenta according to the “heavy-MS” scenario (e.g., from direct collapse channels) adopted from [Ricarte & Natarajan \(2018\)](#). This prediction is derived from a semi-analytic model which traces the evolution of heavy seeds under the assumption of a steady-state accretion model that reproduces the observed AGN main-sequence. This resulting occupation fraction is broadly consistent with studies from cosmological simulations ([Bellovary et al. 2019](#)).

(iii) **Light seed + wanderers:** We adopt an occupation fraction anchored to the [Sicilia et al. \(2022\)](#) BH mass function (BHMF) derived from ongoing stellar formation channels. The [Sicilia et al. \(2022\)](#) BHMF describes the local IMBH population by anchoring to merger rates derived from gravitational wave (GW) observations by LIGO/VIRGO ([Abbott et al. 2021; Baxter et al. 2021](#)). We assume a smooth transition between these GW anchors to the [Sicilia et al. \(2022\)](#) BHMF at  $M_{\text{BH}} \sim 10^2 M_\odot$  and the BHMF from scenario (i) at  $M_{\text{BH}} \sim 10^4 M_\odot$  as a reasonable model to approximate the wandering and off-nuclear IMBHs that have not yet fallen to the center of the host galaxy. The resulting occupation fraction is broadly consistent with the existing constraints on the luminosity function derived from AGNs, ultra-luminous X-ray sources (ULXs), and XRBs as shown in Figure 1(f).

Scenarios (i) and (ii) both assume a single seeding epoch and subsequent growth of the seed BH to fall onto the black hole-host galaxy mass relation at late times. However, stellar cluster seed formation channels can continuously produce IMBHs as recently pointed by [Natarajan \(2021\)](#). There are considerable theoretical uncertainties in these models arising from the hitherto unknown efficiencies of continual seed formation processes. We will incorporate continual BH formation models in future work. Furthermore, multiple seeding scenarios could simultaneously be at work in the Universe, and this implies that theoretical constraints on the occupation functions do remain uncertain for this reason as well. In this work, however, we pursue a brand new avenue and explore if optical variability can be used to constrain the occupation function. Precisely how the low-redshift occupation fraction traces seeding scenarios at high redshifts is more complex question that requires more detailed interpretation

due to the interplay with accretion physics (Mezcua 2019). Here, we adopt two different scenarios described above (i) and (ii) for nuclear black holes as a way to bracket the possible reasonable outcomes.

For each of the scenarios (i) and (ii), we assign each galaxy a BH or not according to its occupation probability. Therefore, the remaining number of draws is given by,

$$N_{\text{draw},\text{BH}} = N_{\text{draw}} \int_{M_{\star,\text{min}}}^{M_{\star,\text{max}}} \lambda_{\text{occ}}(M_{\star}) dM_{\star}, \quad (3)$$

where  $N_{\text{draw}}$  is given by Equation 2.

### 2.3 Black hole mass scaling relations

In the local universe, the stellar mass of the AGN host galaxy scales with the mass of the central BH as a power-law of the form:

$$\log\left(\frac{M_{\text{BH}}}{M_{\odot}}\right) = \alpha + \beta \log\left(\frac{M_{\star}}{M_{\star}^*}\right). \quad (4)$$

We adopt the relation measured from local broad-line AGNs including dwarf galaxies with  $\alpha = 7.45 \pm 0.08$ ;  $\beta = 1.05 \pm 0.11$ ; with a pivot mass  $M_{\star}^* = 10^{11} M_{\odot}$  (Reines & Volonteri 2015) to obtain BH masses for scenario (i) and (ii). We also include the rms scatter of  $\sim 0.6$  dex in  $M_{\text{BH}}$  in the relation when assigning each galaxy a BH mass.

For the wandering BH population of scenario (iii), we assume an analogous relation between the BH mass and mass of the star cluster containing the IMBH  $M_{\text{SC}}$  to obtain their associated stellar masses:

$$\log\left(\frac{M_{\text{SC}}}{M_{\odot}}\right) = \alpha + \beta \log\left(\frac{M_{\text{BH}}}{M_{\text{BH}}^*}\right). \quad (5)$$

We adopt the best-fit parameters from the relation between the BH mass and mass of the nuclear star cluster (as a proxy for  $M_{\text{SC}}$ ) derived from low-mass nuclear star clusters by Graham (2020) with  $\alpha = 7.70 \pm 0.20$ ;  $\beta = 0.38 \pm 0.06$ ;  $M_{\text{BH}}^* = 10^{7.89} M_{\odot}$  and an intrinsic scatter of  $\sim 0.5$  dex in  $M_{\text{SC}}$ . Although by definition wandering black holes would not all necessarily be found in nuclear star clusters, to first order, we assume that this relation offers a reasonable description for off-nuclear star clusters with wandering IMBHs. For the wandering BH population, we will use  $M_{\text{SC}}$  in place of host galaxy stellar mass  $M_{\star}$  to compute the luminosity from starlight that dilutes the variability.

### 2.4 The Eddington ratio distribution

We adopt a broken power-law distribution for the Eddington luminosity ratio ( $\lambda_{\text{Edd}} \equiv L_{\text{bol}}/L_{\text{Edd}}$ ) probability distribution function to compute the AGN bolometric luminosity  $L_{\text{bol}}$  from this. Specifically, we adopt the commonly used double power-law parameterization (Caplar et al. 2015; Sartori et al. 2015, 2019; Weigel et al. 2017; Pesce et al. 2021; Ananna et al. 2022):

$$\xi(\lambda_{\text{Edd}}) = \xi^* \left[ \left( \frac{\lambda_{\text{Edd}}}{\lambda_{\text{Edd}}^*} \right)^{\delta_1} + \left( \frac{\lambda_{\text{Edd}}}{\lambda_{\text{Edd}}^*} \right)^{\delta_2} \right]^{-1}, \quad (6)$$

where  $\xi(\lambda_{\text{Edd}})$  is the Eddington ratio distribution function (ERDF);  $\lambda_{\text{Edd}}^*$  is the break Eddington ratio; and  $\delta_1$ ;  $\delta_2$  are the shallow and steep power law exponents, respectively.

There is compelling evidence that the red and blue galaxy populations that host central AGN that accrete in different modes. Weigel et al. (2017) found that the radio AGN luminosity function (predominately red host galaxies) are described by a broken power law ERDF

favoring lower accretion rates. On the other hand, the X-ray AGN luminosity function (predominately blue host galaxies) described by a broken power law ERDF is found to favor relatively higher accretion rates. (Weigel et al. 2017) interpret this as evidence for a mass-independent ERDF for red and blue galaxies with radiatively inefficient and efficient accretion modes, respectively. We adopt the best-fit parameters for the high-end slope and break Eddington ratio for the red and blue galaxy populations  $\delta_2$ , and  $\log \lambda^*$  from Weigel et al. (2017), in order to match constraints on the  $z \approx 0$  AGN bolometric luminosity function (e.g., Ajello et al. 2012; Aird et al. 2015). In seed scenario (iii), we assume that the wandering IMBH population produced through stellar formation channels anchored to the Sicilia et al. (2022) BHMF are described by the radio AGN ERDF favoring lower accretion rates, which is broadly consistent with expectations that wandering black holes are expected to have lower accretion rates (Bellovary et al. 2019; Guo et al. 2020b; Ricarte et al. 2021a; Seepaul et al. 2022).

The normalization of the ERDF  $\xi^*$  determines how many of the randomly drawn  $N_{\text{draw},\text{BH}}$  BH mass values are assigned an Eddington ratio. Unlike Weigel et al. (2017), we wish to consider an ERDF normalization that describes the *entire* red and blue galaxy population (rather than separate classes of radio or X-ray selected AGNs). Therefore, our ERDFs must be re-normalized accordingly. We set  $\xi^*$  such that the integral of the ERDF from  $\lambda_{\text{Edd},\text{min}}$  to  $\lambda_{\text{Edd},\text{max}}$  is 1. This means that all  $N_{\text{draw},\text{BH}}$  BH values are assigned an Eddington ratio and we have assumed that it is independent of BH mass. Then, noting that the low-end slope  $\delta_1$  is not well-constrained by the AGN luminosity function for  $\delta_1 < -\alpha_1$  (the low-luminosity end of the luminosity function is then determined by  $\alpha_1$ ; Caplar et al. 2015). We allow  $\alpha_1$  to be a free parameter in our model and adjust it to match the overall variable AGN fraction while maintaining consistency with the AGN luminosity function.

The best-fit parameters for radiatively-efficient AGNs from Weigel et al. (2017) are consistent with the ERDF for low-mass galaxies from Bernhard et al. (2018). Radiatively-efficient, low-mass AGNs dominate in number, and have the largest impact on the luminosity function. Although alternative ERDFs have been proposed (Kauffmann & Heckman 2009), the simple mass-independent broken power-law function is able to adequately reproduce observations once selection effects are accounted for (Jones et al. 2016; Ananna et al. 2022). Finally, we caution that a population of  $z \sim 0$  X-ray obscured Compton thick AGNs may be missing from our entire census and hence absent in the luminosity function as well. We consider the optically-obscured AGN fraction later on in this work before computing the optical-band luminosities.

### 2.5 Model consistency with observational constraints

A schematic detailing our model results using random sampling is shown in Figure 1. To ensure that our model parameters are consistent with all available relevant observational constraints, we compare our model AGN luminosity function to the observed local AGN luminosity function from Hao et al. (2005) and Schulze et al. (2009) measured using Type 1, broad-line AGNs from the Sloan Digital Sky Survey (SDSS; faint end) and the Hamburg/ESO Survey (bright end). The number densities in each bin  $i$  are given by:

$$\phi_i(x) = \frac{n_i}{V(z_{\text{min}}, z_{\text{max}}, \Omega) \times \Delta \log x}, \quad (7)$$

where  $x$  is substituted for the variable of interest e.g.,  $M_{\star}$ ,  $M_{\text{BH}}$ , or  $L_{\text{bol}}$ . We fix the ERDF parameters to reproduce the observed local AGN luminosity function from Ajello et al. (2012) starting with the

best-fit parameters of [Weigel et al. \(2017\)](#) and re-normalizing the ERDF to describe the entire galaxy population. This is in reasonably good agreement with the Type 1 bolometric  $z \approx 0$  AGN luminosity function ([Schulze et al. 2009](#); [Hao et al. 2005](#)). We separately consider a Type 1/Type 2 AGN fraction before computing the observable optical luminosities for the AGN population.

To check for the consistency of our derived luminosity functions with observations at luminosities below  $\sim 10^{42}$  erg s $^{-1}$ , we show the observed luminosity function of ULXs) derived from *Chandra* observations of seven collisional ring galaxies ([Wolter et al. 2018](#)). ULXs are non-nuclear sources with X-ray luminosities in excess of  $10^{39}$  erg s $^{-1}$ , generally thought to be X-ray binaries or neutron stars accreting at super-Eddington rates. However, it is possible that some ULXs are in fact accreting IMBHs (e.g., as noted in [Feng & Soria 2011](#); [Kaaret et al. 2017](#)). Regardless, it is important to check that our model bolometric luminosity function for the wandering IMBH population does not exceed the luminosity functions derived from ULXs as a limiting case. We demonstrate the consistency in Figure 1, by assuming a bolometric correction factor of 1.25 ([Anastasopoulou et al. 2022](#)). We exclude sources with X-ray luminosities below  $10^{39}$  erg s $^{-1}$ , where the sample is incomplete ([Wolter et al. 2018](#)). We normalize the [Wolter et al. \(2018\)](#) (per-galaxy) luminosity function to the number density of  $M_\star \sim 10^6 M_\odot$  ultra-low mass dwarf galaxies of  $\sim 10^{-1}$  Mpc $^{-3}$  ([Baldry et al. 2012](#)), whose IMBHs should dominate the low luminosity end of the BH luminosity function. This comparison should be treated with caution, because the [Wolter et al. \(2018\)](#) sample of massive collisional ring galaxies are not fully representative of all dwarf galaxies, and the normalization of the luminosity function is expected to depend on the star formation rate of the host galaxy ([Grimm et al. 2003](#)).

In addition to ULXs, we show the completeness-corrected luminosity function of X-ray binaries (XRBs) spatially coincident with globular clusters (GCs) in nearby galaxies from [Lehmer et al. \(2020\)](#) assuming a bolometric correction of 1.25 ([Anastasopoulou et al. 2022](#)). Again, we confirm that our predicted luminosity functions do not significantly exceed the observed luminosity function of XRBs in GCs after normalizing the luminosity function to the number density of  $M_\star \sim 10^6 M_\odot$  ultra-low mass dwarf galaxies. Similar caveats exist with this comparison and with that of the ULXs, as the results are also expected to depend on the properties of the star cluster.

As an additional check, we plot the GSMF measured from the SDSS-based NASA Sloan Atlas<sup>1</sup> catalog ([Blanton et al. 2011](#)) of  $z < 0.055$  galaxies, which serves as the parent sample of the existing observational constraints ([Baldassare et al. 2018, 2020](#)) using the spectroscopic survey area of  $\Omega \approx 9380$  deg $^2$  (see [Weigel et al. 2016](#)). The SDSS GSMF is roughly consistent with the [Wright et al. \(2017\)](#) GSMF above  $M_\star \sim 10^{10} M_\odot$  but is highly incomplete below. Deeper catalogs will be required to take advantage of the next generation of optical time-domain imaging surveys.

## 2.6 Optical bolometric corrections

In order to predict the observed (time-averaged) luminosity in a given band  $L_{\text{band}}$ , we need to assume a bolometric correction factor, defined as  $\text{BC}_{\text{band}} = L_{\text{bol}}/L_{\text{band}}$ . Typically, bolometric corrections are inferred from a template quasar spectral energy distribution (SED). However, the disk temperature profile of an IMBH is expected to differ significantly from that of a SMBH accreting at the same Eddington ratio, causing the SED to peak in the extreme UV (e.g., [Cann](#)

[et al. 2018](#)). For this reason, it is inappropriate to use standard AGN or quasar SEDs to explore the IMBH regime (e.g., [Richards et al. 2006](#)). Instead, here we adopt the energetically self-consistent model of [Done et al. \(2012\)](#) that assumes that the emission thermalizes to a color-temperature-corrected blackbody only at large radii for radiatively efficient accretion ( $L_{\text{bol}}/L_{\text{Edd}} > 10^{-3}$ ). This model captures the major components observed in the rest-frame UV/optical in narrow-line Seyfert 1 galaxy SEDs: black-body emission from the outer color-temperature-corrected accretion disk; an inverse Compton scattering of photons from the inner disk model of the soft X-ray excess, and inverse Compton scattering in a corona to produce the power-law tail.

For mass accretion rates  $\dot{m} < \dot{m}_{\text{crit}} \approx \alpha^2 \approx 0.1$ , a radiatively inefficient accretion flow (RIAF) is expected to develop, resulting in a much lower luminosity ([Fabian & Rees 1995](#); [Narayan & Yi 1994, 1995](#)). It is thought that black holes with  $10^{-6} < \dot{m} < \dot{m}_{\text{crit}}$  may fall in a hybrid RIAF regime, while “quiescent” BH with  $\dot{m} < 10^{-6}$  are in a RIAF-dominated regime ([Ho 2009](#)), resulting in a power-law SED like the quiescent-state of Sgr A\* ([Narayan et al. 1998](#)). The dimensionless mass accretion rate is given by:

$$\dot{m} \simeq 0.7 (\alpha/0.3) (L_{\text{bol}}/L_{\text{Edd}})^{1/2}, \quad (8)$$

where  $\alpha$  is the [Shakura & Sunyaev \(1973\)](#) viscosity parameter. For RIAFs where,  $L_{\text{bol}}/L_{\text{Edd}} < 10^{-3}$ , we adopt the model of [Nemmen et al. \(2014\)](#). The model includes an inner advection-dominated accretion flow (ADAF), and an outer truncated thin accretion disk and a jet ([Nemmen et al. 2014](#); [Yuan et al. 2007, 2005](#)). This model provides a reasonable description for low luminosity AGNs and low-ionization nuclear emission-line region (LINER; [Eracleous et al. 2010](#); [Molina et al. 2018](#)) galaxies with low accretion rates ( $L_{\text{bol}}/L_{\text{Edd}} \sim 10^{-6} - 10^{-4}$ ; [Nemmen et al. 2014](#)). Therefore, we adopt  $L_{\text{bol}}/L_{\text{Edd}} = 10^{-3}$  as the boundary between radiatively efficient and inefficient accretion flow SEDs, although precisely where this boundary lies is unclear (e.g., [Ho 2009](#)).

### 2.6.1 Radiatively Efficient Accretion

To derive bolometric corrections, we use version 12.12.0 of the xspec software<sup>2</sup> ([Arnaud 1996](#)) to generate a fine grid of [Done et al. \(2012\)](#) optxagnf SED models spanning  $M_{\text{BH}} = 10^2 - 10^9 M_\odot$ ,  $L_{\text{bol}}/L_{\text{Edd}} = 10^{-3} - 1$ , and  $z = z_{\text{min}} - z_{\text{max}}$ . We make the following simple assumptions for the additional parameters in the model: BH spin  $a_\star = 0$ ; coronal radius of transition between black-body emission to a Comptonised spectrum  $r_{\text{cor}} = 100 R_g$ ; electron temperature of the soft Comptonisation component (soft X-ray excess)  $kT_e = 0.23$  keV; optical depth of the soft excess  $\tau = 11$ ; spectral index of the hard Comptonisation component  $\Gamma = 2.2$ ; and fraction of the power below  $r_{\text{cor}}$  which is emitted in the hard Comptonisation component  $f_{\text{pl}} = 0.05$ . The outer radius of the disk is set to the self gravity radius ([Laor & Netzer 1989](#)). These parameters are chosen to roughly match that of narrow-line Seyfert 1 galaxy RE1034+396 (see [Done et al. \(2012\)](#) for a more complete description of each parameter). We interpolate this grid of SEDs at each  $N_{\text{draw},\text{BH}}$  Eddington ratio, BH mass, and redshift using our Monte Carlo model. We provide this grid of pre-calculated SEDs as a supporting fits data file<sup>3</sup>. The format of the data file is described in Table 2. We assume no dust extinction/reddening, because the LSST Rubin wide-fast-deep survey is expected to largely avoid the galactic plane and the intrinsic

<sup>1</sup> <http://nsatlas.org/data>

<sup>2</sup> <https://heasarc.gsfc.nasa.gov/xanadu/xspec/>

<sup>3</sup> <https://doi.org/10.5281/zenodo.6812008>

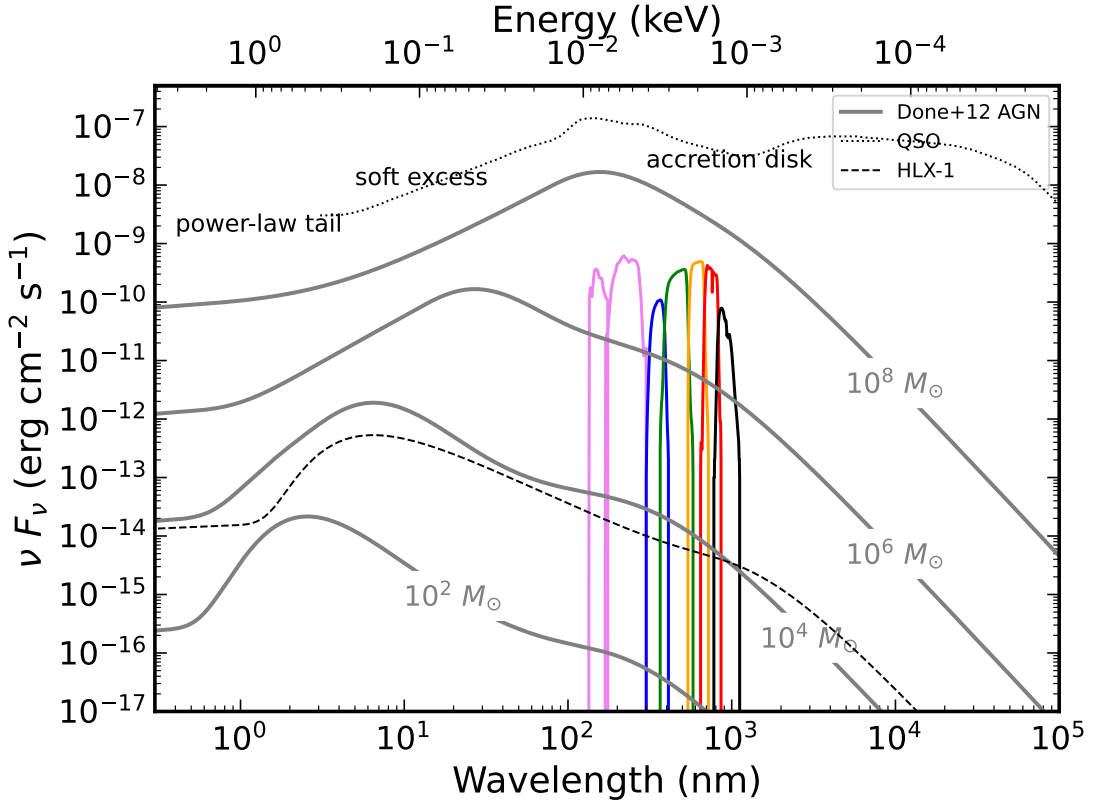


**Figure 2.** Example spectral energy distributions (SEDs) of AGNs with BH masses in the range  $M_{\text{BH}} = 10^2 - 10^8 M_{\odot}$  with  $L_{\text{bol}}/L_{\text{Edd}} = 0.1$  using the model of Done et al. (2012) (thick gray lines, denoted “Done+12 AGN”). We assume a distance of 30 Mpc for these models. We also show the filter transmittance (throughput) curves for the GALEX (FUV and NUF; violet) and SDSS bandpasses (*ugriz*; blue to black) for reference (arbitrary  $y$ -axis scaling). We label the approximate locations of the dominant SED component in black text (but note the shift of their peak wavelengths to the left as  $M_{\text{BH}}$  decreases). The dashed black line is the best-fit Gierliński et al. (2009) irradiated disk model of the IMBH candidate HLX-1 ( $M_{\text{BH}} \sim 10^4 M_{\odot}$ ; Farrell et al. 2014), re-scaled to a distance of 30 Mpc and  $L_{\text{bol}}/L_{\text{Edd}} \sim 0.1$  for comparison (denoted “HLX-1”). The dotted black line is the Type 1 quasar SED of Richards et al. (2006) for SMBHs derived from composite observations (denoted “QSO”). Note the Richards et al. (2006) SED contains emission from the AGN torus at  $> 1$  microns (i.e., the IR bump), while the xspec SEDs do not contain the torus emission.

**Table 2.** Format of the FITS file containing the pre-computed grid of Done et al. (2012) or Nemmen et al. (2014) model SEDs.

Header	Column Name	Format	Unit	Description
0	data	<sup>a</sup> float64	$\log_{10}(\text{erg cm}^{-2} \text{ s}^{-1})$	$\log_{10}$ of the SED computed on the grid
1	data	<sup>b</sup> float64	AB mag	Absolute magnitude in the $i$ band at $z = 2$ computed on the grid
2	log_M_BH	float64	$\log_{10}(M_{\odot})$	$\log_{10}$ of the black hole mass
2	log_LAMBDA_EDD	float64	$\log_{10}(M_{\odot})$	$\log_{10}$ of the Eddington ratio
2	Z	float64		Redshift
3	<sup>c</sup> log_WAV	float64	$\log_{10}(\text{nm})$	$\log_{10}$ of the rest-frame wavelengths where SED is evaluated

<sup>a</sup> This is a 4-dimensional array of the shape  $[\log_{10} M_{\text{BH}}, \log_{10} \text{LAMBDA\_EDD}, Z, \log_{10} \text{WAV}]$ .

<sup>b</sup> This is a 2-dimensional array of the shape  $[\log_{10} M_{\text{BH}}, \log_{10} \text{LAMBDA\_EDD}]$ .

<sup>c</sup> The wavelength range over which the SEDs are evaluated is  $10^{-3} - 10^8$  nm spaced evenly in log space.

dust extinction in Type 1 AGNs is generally small. Finally, we use the optical filter transmission curves and the SED to compute  $L_{\text{band}}$ . The Done et al. (2012) SED models are undefined for  $M_{\text{BH}} > 10^9 M_{\odot}$  in xspec, so we caution that our derived luminosities for the most massive SMBHs relies on extrapolation from this grid of parameters. Nevertheless, we will show that our derived  $L_{\text{band}}$  values are close to the observed  $L_{\text{band}}$  values from SDSS quasars below.

We show Done et al. (2012) model SEDs spanning  $M_{\text{BH}} = 10^2 - 10^8 M_{\odot}$  with  $L_{\text{bol}}/L_{\text{Edd}} = 0.1$  in Figure 2. Our model SEDs are evaluated on a grid spanning  $M_{\text{BH}} = 10^2 - 10^9 M_{\odot}$ , but we have only shown a subset of the results to avoid crowding the figure. We over-plot the SDSS optical (Blanton et al. 2017) and GALEX UV (Martin et al. 2005) filter transmission curves for reference. For comparison, we also show the best-fit Gierliński et al. (2009)

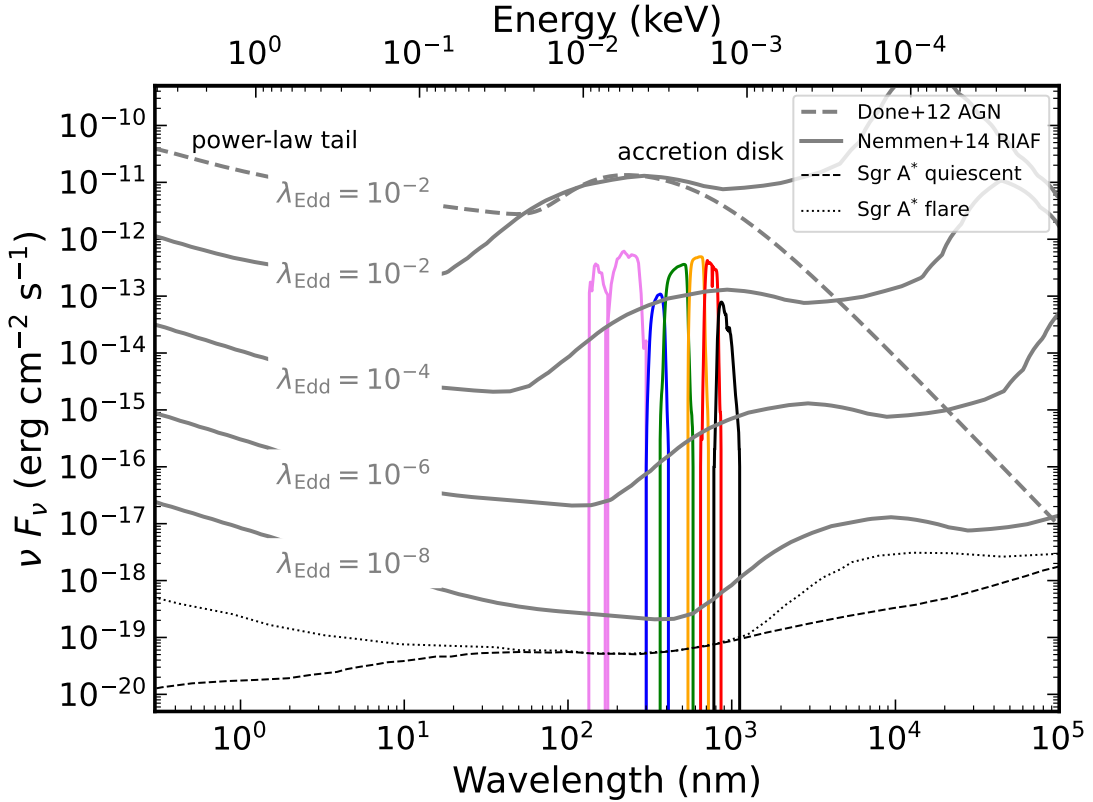


**Figure 3.** Template RIAF spectral energy distributions (SEDs) of AGNs with Eddington luminosity ratios in the range  $\lambda_{\text{Edd}} \equiv L_{\text{bol}}/L_{\text{Edd}} = 10^{-8} - 10^{-2}$ , with  $M_{\text{BH}} = 4 \times 10^6 M_{\odot}$  using the model of Yuan et al. (2003) as implemented by Nemmen et al. (2014) (thick gray lines, denoted “Nemmen+14 RIAF”). For comparison, we show the radiatively efficient accretion model of Done et al. (2012) using the same parameters in Figure 2, except we set the electron temperature for the soft Comptonisation component to  $kT_e = 1.9$  keV to match Sgr A\* (Baganoff et al. 2003) (thick dashed gray lines, denoted “Done+12 AGN”). We assume a distance of 30 Mpc for these models. We also show the filter transmittance (throughput) curves for the GALEX (FUV and NUV; violet) and SDSS bandpasses ( $ugriz$ ; blue to black) for reference (arbitrary y-axis scaling). We label the approximate locations of the dominant SED component in black text (but note the shift of their peak wavelengths to the right as  $\lambda_{\text{Edd}}$  decreases). The dashed (dotted) black line is the best-fit quiescent-state (flaring-state) Yuan et al. (2003) radiatively inefficient accretion flow disk model for Sgr A\* ( $\lambda_{\text{Edd}} \sim 10^{-8.5}$ ;  $M_{\text{BH}} = 4.3 \pm 0.2 \times 10^6 M_{\odot}$ ; Genzel et al. 2010), assuming a distance of 30 Mpc. Note the Yuan et al. (2003) SED contains outflow/jet synchrotron low-frequency radio emission, while the Done et al. (2012) xspec SEDs do not contain the outflow/jet synchrotron emission.

irradiated disk model of the IMBH candidate HLX-1 (Farrell et al. 2009) fit to *Hubble Space Telescope* and *Swift* photometry from Farrell et al. (2014). This SED model displays qualitatively similar features to the Done et al. (2012) models, given its expected mass of  $M_{\text{BH}} \sim 10^4 M_{\odot}$  and distance of 95 Mpc (Farrell et al. 2014). Other phenomenological models might also adequately describe the SED arising from an accretion-disk around an IMBH (e.g., Mitsuda et al. 1984; Makishima et al. 1986). Indeed the SED from the accretion disk emission may differ if the IMBH is in a binary configuration that undergoes state transitions similar to X-ray binaries (Servillat et al. 2011). Here, we assume an IMBH is in a “high-soft”/rapidly-accreting state where its disk may be approximately geometrically thin and behave like a scaled-down accretion disk around a SMBH (McHardy et al. 2006; Scaringi et al. 2015; Burke et al. 2021c). One could also incorporate variations in model parameters into our Monte Carlo framework. Although our results depend on these model assumptions, it is unlikely to change our final results in excess of the fiducial uncertainty on the BH mass/bolometric luminosity function. Nevertheless, we retain the flexibility in our framework to substitute other SED models as better observational constraints on dwarf AGN SEDs become available in the future.

## 2.6.2 Radiatively Inefficient Accretion

We calculate Nemmen et al. (2014) RIAF model SEDs<sup>4</sup> and add them to our grid of model SEDs spanning  $M_{\text{BH}} = 10^2 - 10^9 M_{\odot}$ ,  $L_{\text{bol}}/L_{\text{Edd}} = 10^{-8} - 10^{-3}$ , and  $z = z_{\text{min}} - z_{\text{max}}$ . We make the following simple assumptions for the additional parameters in the model: power-law index for accretion rate (or density) radial variation  $s = 0.3$ , Shakura & Sunyaev (1973) viscosity parameter  $\alpha = 0.3$ , ratio between the gas pressure and total pressure  $\beta = 0.9$ , strength of wind  $p = 2.3$ , fraction of energy dissipated via turbulence that directly heats electrons  $\delta = 10^{-3}$ , adiabatic index  $\gamma = 1.5$ . The outer radius of the disc is set to the self gravity radius (Laor & Netzer 1989). These parameters are chosen to roughly match those inferred from fitting a sample of LINERs from Nemmen et al. (2014) (see the Nemmen et al. paper for a more complete description of each parameter). To overcome sensitivities to boundary conditions when finding model solutions, we generate a single template SED with Sgr A\*-like parameters and normalize the resulting SED by BH mass

<sup>4</sup> <https://github.com/rsnemmen/riaf-sed>

and accretion rate. We then include the simple color-temperature correction analogous to Done et al. (2012).

We show Nemmen et al. (2014) RIAF SEDs spanning  $L_{\text{bol}}/L_{\text{Edd}} = 10^{-8} - 10^{-2}$  along with a Done et al. (2012) SED with  $L_{\text{bol}}/L_{\text{Edd}} = 10^{-2}$  with  $M_{\text{BH}} = 4 \times 10^6 M_{\odot}$  in Figure 3 and  $kT_e = 1.9 \text{ keV}$  to match Sgr A\* (Baganoff et al. 2003). For comparison, we show the SED of Sgr A\* ( $\lambda_{\text{Edd}} \sim 10^{-8.5}$ ;  $M_{\text{BH}} = 4.3 \pm 0.2 \times 10^6 M_{\odot}$ ; Genzel et al. 2010) in both its quiescent and flaring states and using the radiatively inefficient accretion flow disk model of Yuan et al. (2003). We find the Nemmen et al. (2014) models provide a reasonable approximation to the optical/UV/X-ray emission of the flaring-state SED of Sgr A\*. The difference in the shape of the SED compared to Done et al. (2012) model SEDs is attributed to differences between radiatively efficient and RIAFs cooled by advection (Narayan & Yi 1994, 1995). There are many theoretical uncertainties regarding the nature of RIAFs, owing to a lack of high-quality observations. However, these detailed assumptions will only affect the luminosities for sources with very low accretion rates in our model which fortunately do not dominate the variability-selected samples.

## 2.7 Optical variability

To a good approximation, AGN light curves can be well described by a damped random walk (DRW) model of variability (Kelly et al. 2009; MacLeod et al. 2010). We assume a DRW model for both accretion modes. In the DRW model, the PSD is described by a  $f^{-2}$  power-law at the high-frequency end, transitioning to a white noise at the low-frequency end. The transition frequency corresponds to the damping timescale  $\tau_{\text{DRW}}$  as  $f_0 = 1/(2\pi\tau_{\text{DRW}})$ . The damping timescale thus describes a characteristic timescale of the optical variability. There is growing evidence that the variability characteristics depend on AGN properties. Burke et al. (2021b) found that (i) the damping timescale depends on accretor mass and (ii) there exists a strong correlation between  $\tau_{\text{DRW}}$  and BH mass, which extends to the stellar mass range using optical variability measured for nova-like accreting white dwarfs (Scaringi et al. 2015). We generate mock AGN light curves using the recipe of MacLeod et al. (2010); Suberlak et al. (2021):

$$\log \left( \frac{\text{SF}_{\infty}}{\text{mag}} \right) = A + B \log \left( \frac{\lambda_{\text{RF}}}{4000 \text{ \AA}} \right) + C (M_i + 23) + D \log \left( \frac{M_{\text{BH}}}{10^9 M_{\odot}} \right), \quad (9)$$

where  $A = -0.51 \pm 0.02$ ,  $B = -0.479 \pm 0.005$ ,  $C = 0.131 \pm 0.008$ , and  $D = 0.18 \pm 0.03$ ; and,

$$\log \left( \frac{\tau}{\text{days}} \right) = A + B \log \left( \frac{\lambda_{\text{RF}}}{4000 \text{ \AA}} \right) + C (M_i + 23) + D \log \left( \frac{M_{\text{BH}}}{10^9 M_{\odot}} \right), \quad (10)$$

where  $\text{SF}_{\infty}$  is the structure function (SF) evaluated at infinity (i.e., asymptotic rms variability amplitude; e.g., Kozłowski 2016) and  $A = 2.4 \pm 0.2$ ,  $B = 0.17 \pm 0.02$ ,  $C = 0.03 \pm 0.04$ , and  $D = 0.21 \pm 0.07$  (Suberlak et al. 2021). Here we adopt the coefficients of  $A = 2.029 \pm 0.004$ ,  $D = 0.38 \pm 0.05$  and pivot mass from Burke et al. (2021b) which includes dwarf AGNs. In these relations,  $\lambda_{\text{RF}}$  is the rest-frame wavelength of the observation, i.e.,  $\lambda_{\text{RF}} = \lambda_{\text{obs}}/(1+z)$  where  $\lambda_{\text{obs}}$  is the central wavelength of the filter/band and  $z$  is the redshift, and  $M_i$  refers to the  $i$ -band absolute magnitude  $K$ -corrected to  $z = 2$ ,  $M_i(z=2)$ , as a proxy for the AGN bolometric luminosity  $L_{\text{bol}}$  following Richards et al. (2006). As such, we adopt the relation

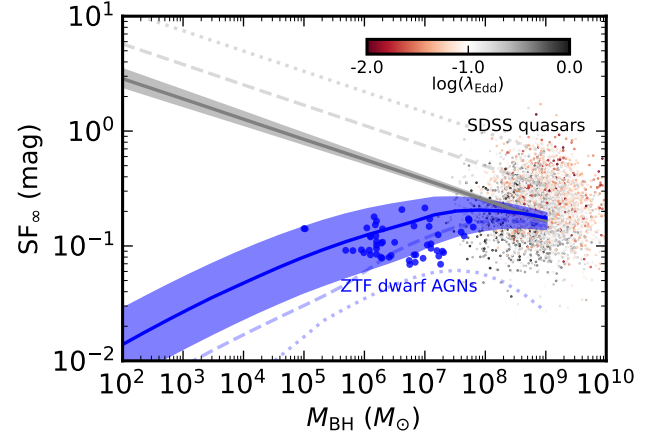


**Figure 4.** Asymptotic rms variability amplitude  $\text{SF}_{\infty}$  versus virial BH mass  $M_{\text{BH}}$  for the sample of SDSS quasars measured from SDSS light curves (points colored by their Eddington luminosity ratios  $\lambda_{\text{Edd}}$ ; MacLeod et al. 2010) and broad-line dwarf AGNs (blue circle symbols) measured from ZTF light curves in the  $g$  band computed at  $z \sim 0.01$ . The extrapolated  $\text{SF}_{\infty}$  relations from the MacLeod et al. (2010) prescription (Equation 9) assuming no host galaxy dilution are shown in gray with  $L_{\text{bol}}/L_{\text{Edd}} = 0.1$  (solid line), 0.01 (dashed line), and 0.001 (dotted line) with  $1\sigma$  uncertainty band shown over the  $L_{\text{bol}}/L_{\text{Edd}} = 0.1$  prediction. Our modified extrapolations are similarly shown in blue after accounting for host galaxy dilution assuming a color index of  $g-r = 0.5$  and a covering factor of  $f_{\star} = 10\%$ , typical of low-redshift dwarf galaxies. The inconsistency (opposite trends) with the  $L_{\text{bol}}/L_{\text{Edd}}$  scaling for SDSS quasars and our model is due to the dimming of AGN light as  $L_{\text{bol}}/L_{\text{Edd}}$  decreases, leading to more host dilution. We have also assumed different host galaxy colors compared to quasar host galaxies (e.g., Matsuoka et al. 2014), and the dwarf galaxy and SDSS quasar populations are at different redshifts. The uncertainty is dominated by scatter in the BH-host galaxy relation and the galaxy mass-to-light ratio (see §2.7). Our modified relation gives more reasonable results in the IMBH regime and is more consistent with observations of dwarf AGN variability. Typical uncertainties on the  $\text{SF}_{\infty}$  measurements are  $\sim 0.1$  dex. Virial mass uncertainties are typically  $\sim 0.4$  dex (e.g., Shen 2013).

$M_i = 90 - 2.5 \log(L_{\text{bol}} / \text{erg s}^{-1})$  (Shen et al. 2009) instead of the actual value computed from the SED (Figure 6) in these relations so that this variable still acts as a linear proxy for  $\log L_{\text{bol}}$  when extrapolated to low BH masses.

We show the predicted  $g$ -band  $\text{SF}_{\infty}$  versus  $M_{\text{BH}}$  in Figure 4 using the Done et al. (2012) SEDs to compute  $M_i$  (Figure 6) and varying  $L_{\text{bol}}/L_{\text{Edd}} = 0.1$ , 0.01, and 0.001. Similarly, we show results for varying host galaxy dilution covering factors of  $f_{\star} = 0.2\%$ , 2%, 20%, and 100% in Figure 5. For context, we show the individual data points from SDSS quasars (MacLeod et al. 2010) and dwarf AGNs with broad-line (virial) BH mass estimates and  $\text{SF}_{\infty}$  values measured from Zwicky Transient Facility (ZTF; Bellm et al. 2019) light curves (Burke et al. in prep). We extrapolate the MacLeod et al. (2010) relation to the IMBH regime, but find the predicted  $\text{SF}_{\infty}$  values of  $\gtrsim 1$  mag are far too large to be reasonable. An IMBH with this level of variability has not been detected. The MacLeod et al. (2010) sample is dominated by quasars, so  $M_i$  and  $\text{SF}_{\infty}$  correspond primarily to emission from the quasar with a small component contributed by host galaxy. However, in the IMBH regime, host galaxy light is expected to dominate, diluting the variability amplitude from the AGN emission. To estimate this host galaxy light dilution, we use the  $M_{\text{BH}} - M_{\star}$  relation of Reines & Volonteri (2015) (Equation 4)

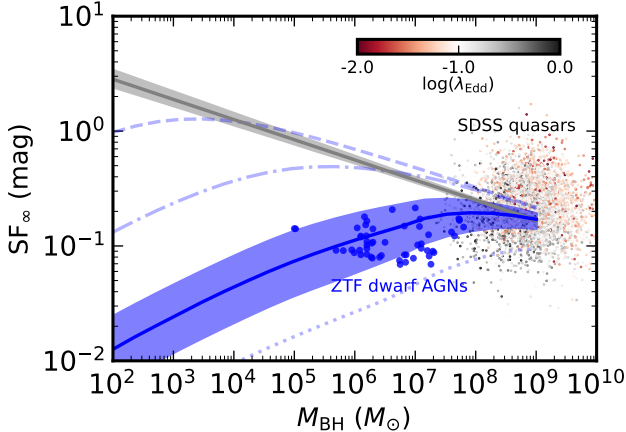


**Figure 5.** Same as Figure 4 but with  $L_{\text{bol}}/L_{\text{Edd}} = 0.1$  and varying host dilution covering factors of  $f_{\star} = 0.2\%$  (dashed line),  $2\%$  (dash-dotted line),  $20\%$  (solid line), and  $100\%$  (dotted line) with  $1\sigma$  uncertainty band shown over the  $f_{\star} = 20\%$  prediction. The results with no host dilution are a reasonable approximation of the extrapolated relation for quasars (MacLeod et al. 2010).

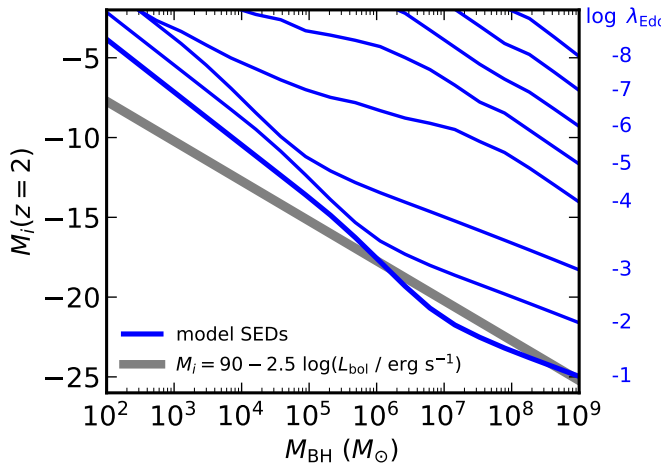


**Figure 6.** Absolute  $i$ -band magnitude  $K$ -corrected to  $z = 2$  versus BH mass computed with the Done et al. (2012) ( $L_{\text{bol}}/L_{\text{Edd}} > 10^{-3}$ ) or Nemmen et al. (2014) ( $L_{\text{bol}}/L_{\text{Edd}} < 10^{-3}$ ) SEDs (blue) compared to the relation for quasars  $L_{\text{bol}}/L_{\text{Edd}} = 0.1$  (gray; e.g., Shen et al. 2009). The thick blue line is the  $L_{\text{bol}}/L_{\text{Edd}} = 0.1$  case, while the thin blue lines span  $L_{\text{bol}}/L_{\text{Edd}} = 10^{-2} - 10^{-8}$ . The width of the gray line corresponds to the  $1\sigma$  scatter in the relation. The more complex shape of the blue curve—namely, larger  $M_i(z=2)$  at lower BH mass—is due to the blueward disk temperature shift at lower BH masses. For  $M_{\text{BH}} < 10^6 M_{\odot}$ , this relation is well-approximated by  $M_i = 125 - 3.3 \log(L_{\text{bol}} / \text{erg s}^{-1})$ .

and the stellar mass-to-light ratios of Zibetti et al. (2009) assuming a host galaxy color index typical of dwarf AGNs of  $g - r \approx 0.5$  (e.g., Baldassare et al. 2020; Reines et al. 2013) and contamination factor of  $f_{\star} = 20\%$  (i.e., covering factor, accounting for aperture effects) such that the host galaxy luminosity enclosed in an aperture is  $L_{\star, \text{ap}} = f_{\star} L_{\star}$ , where  $L_{\star}$  is the total luminosity from the host galaxy starlight. These assumptions are justified further in Appendix B, and

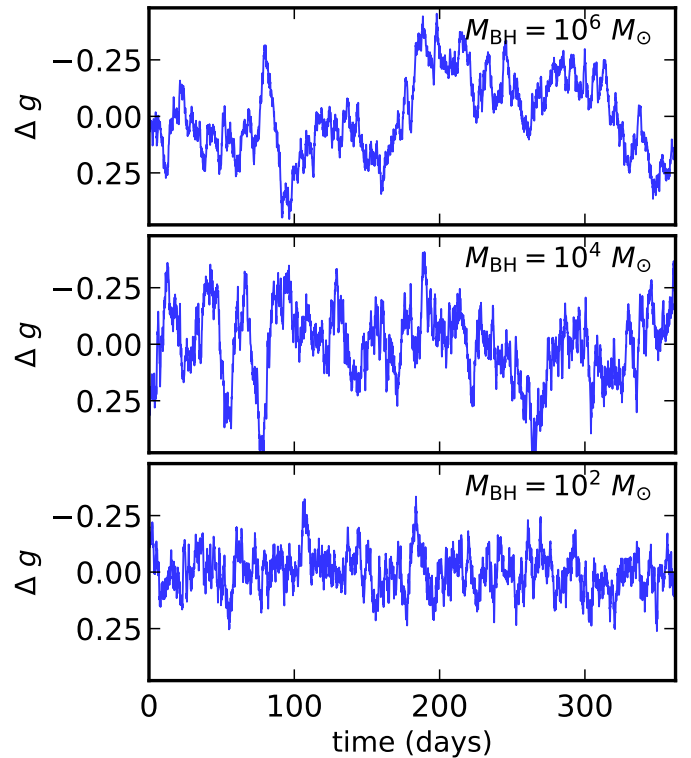


**Figure 7.** Example mock DRW  $g$ -band rest-frame light curves of AGNs with BH masses in the range  $M_{\text{BH}} = 10^2 - 10^6 M_{\odot}$ ,  $L_{\text{bol}}/L_{\text{Edd}} = 0.1$ ,  $g - r = 0.5$  and a host dilution covering factor of  $f_{\star} = 10\%$ , with a duration of 1 year. The mock light curve prescription includes estimates of host galaxy contamination following §2.7. The variability amplitude of an IMBH saturates at a few tenths of a magnitude due to host dilation and the characteristic timescale of variability is  $\sim$  tens of hours.

we will use these mass-dependent parameterizations of the color index and covering factor in our final model. The resulting observed (diluted) rms variability amplitude is,

$$\text{SF}'_{\infty} = \frac{L_{\text{AGN}}}{L_{\text{AGN}} + f_{\star} L_{\star}} \text{SF}_{\infty}, \quad (11)$$

where  $L_{\text{AGN}}$  is the mean AGN luminosity (assumed to be a point source),  $L_{\star}$  is the host galaxy luminosity in a given band, and  $\text{SF}_{\infty}$  is given by Equation 9.

We caution that the assumptions above are highly uncertain (e.g.,  $\sim 0.5$  dex scatter in the  $M_{\text{BH}} - M_{\star}$  relation and  $\sim 0.3$  dex scatter in the mass-to-light ratios) and the level of host contamination would depend on the individual galaxy. Nevertheless, these qualitative arguments yield more reasonable predictions for the variability amplitude in the IMBH regime and are surprisingly consistent with observations of dwarf AGN variability which have typical  $\text{SF}_{\infty}$  values of a few tenths of a magnitude (Baldassare et al. 2018, 2020; Burke et al. 2020; Ward et al. 2020; Martínez-Palomera et al. 2020). Our modified relation also gives a reasonable prediction for low Eddington ratio black holes. When the AGN emission dominates, the observed anti-correlation between Eddington ratio and variability amplitude (e.g., Wilhite et al. 2008; Simm et al. 2016; Caplar et al. 2017; Rumbaugh et al. 2018) may hold for quasars ( $M_{\text{BH}} \sim 10^8 - 10^{10} M_{\odot}$ ;  $L_{\text{bol}}/L_{\text{Edd}} \sim 0.1$ ), but below a certain Eddington ratio, the host galaxy dilution becomes so large as to swamp the AGN variability

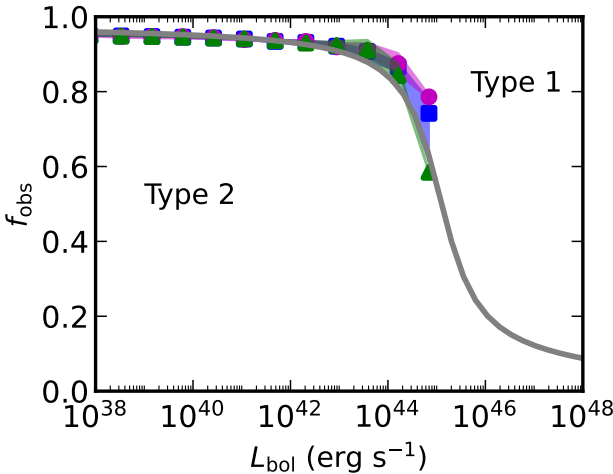


**Figure 8.** Fraction of optically obscured AGNs  $f_{\text{obs}}$  as a function of bolometric luminosity. The gray line shows the model of Merloni et al. (2014) using the X-ray bolometric correction of Duras et al. (2020). The colored points and  $1\sigma$  uncertainty bands are shown for the input “light” (blue/square symbols), “heavy” (magenta/circle symbols), and “light + wanderers” (green triangle symbols) seeding scenarios probed for our LSST-like model.

entirely. This is consistent with the lack of detected strong optical variability in very low luminosity AGNs (e.g., detected by ultra deep radio or X-ray surveys) due to host dilution.

We show sample mock DRW  $g$ -band light curves of AGNs (including host dilution following the prescription above) with BH masses in the range  $M_{\text{BH}} = 10^2 - 10^8 M_{\odot}$  with  $L_{\text{bol}}/L_{\text{Edd}} \sim 0.1$  in Figure 7 with the same assumptions as above. This figure demonstrates the dramatically more rapid variability ( $\lesssim$  days) shown by AGNs in the IMBH regime and suppressed variability amplitude due to estimated host dilution. We compute full mock DRW light curves for all the  $N_{\text{draw,BH}}$  sources in our Monte Carlo model and adopt a simple stellar mass-dependent  $g - r$  color index and redshift-dependent contamination factor based on a fitting to SDSS NASA Sloan Atlas galaxies as described in the Appendix B. We assume the emission from the stellar mass of the host star clusters of the wanderers in scenario (iii) are unresolved. This is consistent with the typical size of young star clusters in the local Universe of a few pc or less (Carlson & Holtzman 2001).

## 2.8 Optical Type 1 fraction

Type 2 (highly optically obscured) AGNs show little or no detectable optical variability because their UV/optical accretion disk emission is thought to be obscured (Barth et al. 2014). We adopt the luminosity-dependent optically obscured AGN fraction  $f_{\text{obs}}$  from Merloni et al. (2014):

$$f_{\text{obs}}(l_x) = A + \frac{1}{\pi} \tan^{-1} \left( \frac{l_0 - l_x}{\sigma_x} \right), \quad (12)$$

where  $l_x = \log(L_X/\text{erg s}^{-1})$  and their best-fit parameters from their X-ray selected sample are  $A = 0.56$ ,  $l_0 = 43.89$ , and  $\sigma_x = 0.46$ . However, we adopt the normalization  $A = 0.5$  to ensure  $f_{\text{obs}}$  asymptotes to unity at low luminosity. Formal uncertainties are not given by Merloni et al. (2014), but the uncertainties in their luminosity bins

are  $\sim 0.2$  dex in luminosity. We show the optically-obsured fraction as function of  $L_{\text{bol}}$  in Figure 8 using the luminosity-dependent 2–10 keV bolometric correction of Duras et al. (2020). We randomly assign each  $N_{\text{draw,BH}}$  sources in our Monte Carlo model to be optically obscured or unobscured using the probability function shown in Figure 8. We simply set the AGN luminosity to zero for optically obscured sources, with Equation 11 ensuring their variability would be undetectable ( $\text{SF}'_{\infty} \approx 0$  for  $L_{\text{AGN}}/f_{\star} L_{\star} \ll 1$ ).

## 3 MOCK OBSERVATIONS

### 3.1 Light curves

In order to perform source forecasts, we generate synthetic observations assuming LSST Rubin -like observational parameters. We focus our mock observations on the  $g$ -band, because the (diluted) AGN variability amplitude is typically larger at bluer wavelengths and the  $u$ -band suffers from worse single-epoch imaging depth. We generate realistic DRW light curves with a duration of 10 years, a cadence of 25 days, and a season length of 150 days, which roughly matches the expected median values of the “baseline”  $g$ -band LSST Rubin wide-fast-deep survey.<sup>5</sup> We adopt the photometric precision model of LSST Rubin from Ivezić et al. (2019) of the form:

$$\sigma_1^2 = \sigma_{\text{sys}}^2 + \sigma_{\text{rand}}^2, \quad (13)$$

where  $\sigma_1$  is the expected photometric error in magnitudes for a single visit,  $\sigma_{\text{sys}}$  is the systematic photometric error, and  $\sigma_{\text{rand}}$  is the random photometric error given by,

$$\sigma_{\text{rand}}^2 = (0.04 - \gamma) x + \gamma x^2 (\text{mag}^2) \quad (14)$$

with  $x \equiv 10^{0.4(m-m_5)}$  where  $m_5$  is the  $5\sigma$  limiting magnitude for point sources in a given band, and  $\gamma$  is a band-dependent parameter which depends on sky brightness and instrument properties. We use the expected  $g$ -band flux limit of  $m_5 = 25.0$  mag,  $\sigma_{\text{sys}}^2 = 0.005$  mag, and  $\gamma = 0.039$  (Ivezić et al. 2019), which is in good agreement with mock observations from synthetic data (Sánchez et al. 2020). In order to enable comparison with the current observational constraints (Baldassare et al. 2020), we generate similar mock observations with the PTF (Law et al. 2009). We adopt a cadence of 5 days, a season length of 100 days, and a total survey length of 5 years. We use the same photometric precision model from Ivezić et al. (2019) but with an  $R$ -band flux limit now of  $m_5 = 21.5$  mag,  $\sigma_{\text{sys}}^2 = 0.005$  mag, and  $\gamma = 0.035$ . We obtained these values that approximate the data in Figure 3 of Baldassare et al. (2020) by eye. This is apparently more precise at fixed magnitude than the (Ofek et al. 2012) PTF calibration. We show the photometric precision models and measured light curve rms values for LSST Rubin and the PTF in Figure 9.

Taking our mock light curves with flux-dependent uncertainties, we then use the simple  $\chi^2$ -based variability metric to compute the variability significance:

$$\left[ \chi^2/\nu \right]_{\text{var}} = \frac{1}{\nu} \sum_{i=1}^N (m_i - \bar{m})^2 w_i, \quad (15)$$

where the weighted mean  $\bar{m}$  is given by,

$$\bar{m} = \frac{\sum_{i=1}^N m_i w_i}{\sum_{i=1}^N w_i}, \quad (16)$$

<sup>5</sup> See `baseline_v2.0_10yrs` metrics at <http://astro-lsst-01.astro.washington.edu:8080/allMetricResults?runId=1>

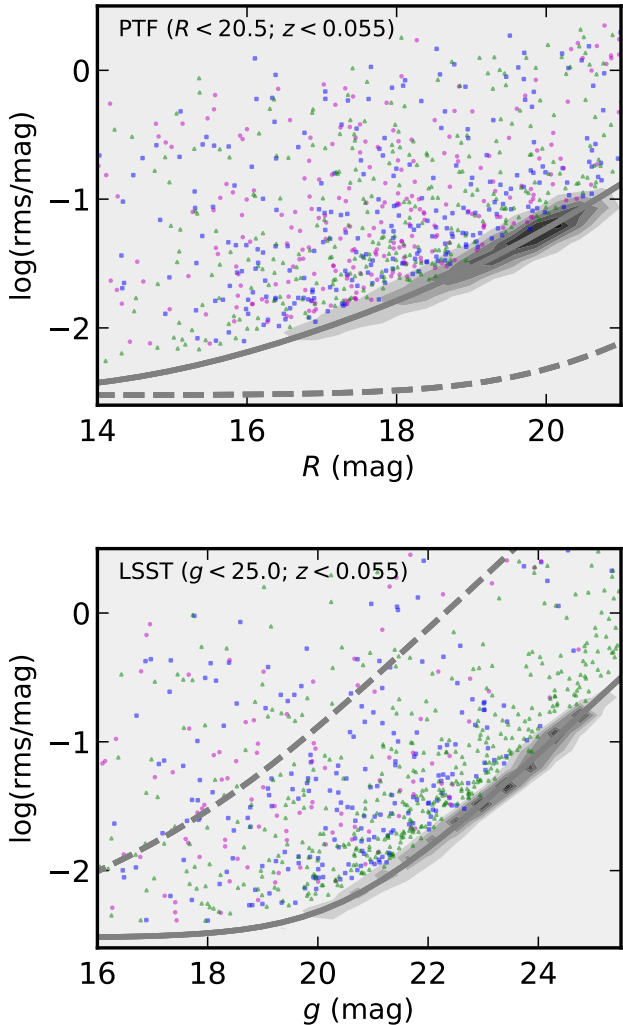


**Figure 9.** Measured light curve rms versus host galaxy aperture magnitude for our PTF (upper panel; cf. Figure 3 of [Baldassare et al. 2020](#)) and LSST-like (lower panel) mock samples. The variable sources are shown as colored points (magenta circles: “heavy” seed scenario; blue squares: “light” seed scenario; green triangles: “light + wanderers” scenario), while the shaded contours shows the total light curve distribution (darker contours being regions of higher density). The distributions are from a single, representative bootstrap realization of our model results. The number of data points has been reduced by a factor of 10 (PTF) or 100 (LSST) to improve clarity. The single-visit model photometric precision rms  $\sigma_1$  versus apparent magnitude for LSST Rubin  $g$ -band following Equations 13 and 14 ([Ivezic et al. 2019](#)) is shown in gray. To facilitate comparison, the dashed lines in the top panel and lower panel show the photometric precision model for LSST Rubin and PTF, respectively.

with weights given by the reciprocal of the squared photo-metric uncertainties  $w_i = 1/\sigma_i^2$  on each measurement  $m_i$  in magnitudes (e.g., [Butler & Bloom 2011](#); [Choi et al. 2014](#)). We then convert this test statistic to a resulting significance  $\sigma_{\text{var}}$  in units of  $\sigma$ . This metric is statistically-motivated, model independent, and fast to compute. Following [Baldassare et al. \(2020\)](#), we consider a source to be variable if its light curve satisfies  $\sigma_{\text{var}} > 2$ , which implies a  $\sim 5\%$  false positive rate. We require the light curve input rms variability amplitude  $\text{SF}_{\infty}$  to be larger than the survey’s photo-metric precision, i.e.,

**Table 3.** Number of expected IMBHs and massive BHs detectable with LSST Rubin over the WFD footprint.

Seeding Scenario	Number IMBHs <sup>a</sup>	Number massive BHs <sup>b</sup>
light (i)	$3.9^{+4.1}_{-3.0} \times 10^2$	$1.5^{+0.6}_{-0.6} \times 10^3$
heavy (ii)	$5.9^{+5.9}_{-5.9} \times 10^0$	$5.9^{+1.5}_{-1.5} \times 10^3$
light + wanderers (iii)	$9.7^{+6.2}_{-6.9} \times 10^3$	$2.1^{+0.5}_{-0.7} \times 10^4$

<sup>a</sup>  $10^2 M_{\odot} < M_{\text{BH}} < 10^4 M_{\odot}$ .

<sup>b</sup>  $10^4 M_{\odot} < M_{\text{BH}} < 10^6 M_{\odot}$ .

$\text{SF}_{\infty} > \sigma_1(m)$ , where  $m$  is the magnitude of the source and  $\sigma_1$  is the photo-metric precision model (Equation 13) to assure that our variable sources are reliable detections. Our model does not include other contaminants, such as other variable transients (e.g., supernovae, tidal disruption events, or variable stars), or other (possibly non-Gaussian) systematic sources of light curve variability (i.e., non-photometric observations). Therefore, we have no need to introduce a classification metric for “AGN-like” variability. This makes our selection simpler and less dependent on the exact underlying process describing AGN light curves but more idealized than reality. We show histograms of the  $\text{SF}_{\infty}$ ,  $\tau$ , and  $\lambda_{\text{Edd}}$  values for our sources in Figure 10, highlighting our detected variable sources from realistic LSST Rubin -like light curves.

### 3.2 Observational Forecasts

We compute the recovered (observed) fraction of variable galaxies in bins of stellar mass and magnitude using the criteria  $\sigma_{\text{var}} > 2$  for both the LSST Rubin ( $g < 25.0$  mag) and the PTF ( $R < 20.5$  mag) in Figure 11. We assume a bright saturation limit of  $R > 14$  mag for the PTF ([Ofek et al. 2012](#)) and  $g > 16$  mag for LSST Rubin ([Ivezic et al. 2019](#)). The uncertainties in the figure trace the uncertainties in the model itself. The slight uptick in the smallest mass bin for the PTF light seed scenario can result from small number statistics, because the smallest bins which only contain a few sources. Recall that we have assumed  $z < 0.055$  and consider a source to be variable if  $\sigma_{\text{var}} > 2$  and the rms variability is larger than the uncertainty given by the photo-metric precision model.<sup>6</sup> We assume total survey solid angles of  $\Omega = 9380 \text{ deg}^2$  and  $\Omega = 18,000 \text{ deg}^2$  for the PTF and LSST Rubin, respectively. We show the distribution of stellar mass versus redshift for a single, representative bootstrap realization of our model results in Figure 12.

We also compute the recovered fraction of variable galaxies versus BH mass for our LSST Rubin-like model in Figure 13, albeit the BH mass is not usually a directly observable quantity. Assuming an LSST Rubin-like footprint of  $\Omega = 18,000 \text{ deg}^2$ , the number of expected IMBHs in the mass range  $10^2 M_{\odot} < M_{\text{BH}} < 10^4 M_{\odot}$  and “massive black holes”  $10^4 M_{\odot} < M_{\text{BH}} < 10^6 M_{\odot}$  using optical variability for the various occupation fractions used in this work are enumerated in Table 3. Similar figures divided into the blue and red galaxy populations is shown in Appendix D. Our calculations indicate that LSST Rubin may be a very promising source for uncovering massive black holes and IMBH candidates modulo the underlying occupation fraction.

<sup>6</sup> One need not necessarily use the rms constraint when constructing a version of Figure 11, although the number of false positive detections would likely increase if this is not done. In fact, the  $\sigma_{\text{var}}$  threshold can be lowered further or a different measure, such as the rolling average  $\sigma_{\text{var}}$  versus stellar mass, could be adopted which may be more sensitive to the input occupation fraction.

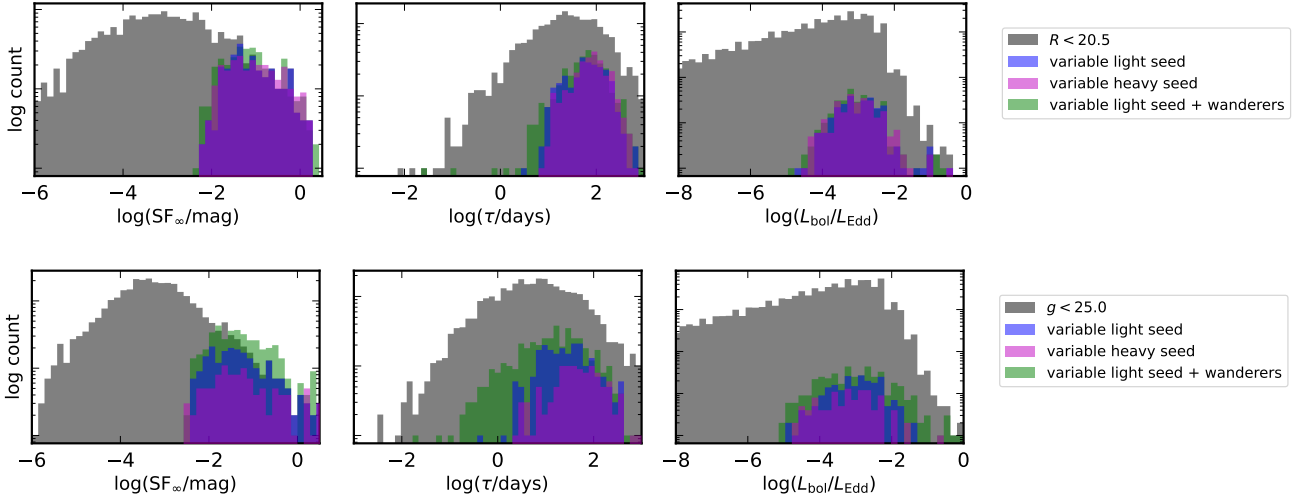


**Figure 10.** Distributions of (host diluted) asymptotic rms variability amplitude  $SF_{\infty}$ , rest-frame damping timescale  $\tau$ , and Eddington luminosity ratios for all sources within the flux limit of the survey (gray) and variable sources detected in the survey for the different input seeding scenarios (magenta: “heavy”; blue: “light”; green: “light + wanderers”) for our PTF (*upper panel*) and LSST-like (*lower panel*) mock samples. The distributions are from a single, representative bootstrap realization of our model results. This figure demonstrates the resulting distributions of the parameters relative to the input distributions after variability selection.

### 3.3 Recoverability of black hole masses from variability timescales

In order to determine how well one can recover the BH mass using optical variability information alone, we attempt to infer the input damping timescale  $\tau$  values using mock light curves using different cadence scenarios. Because the dependence of the damping timescale on wavelength is weak (MacLeod et al. 2010; Suberlak et al. 2021; Stone et al. 2022), observations from multiple bands could be effectively combined to reduce the typical cadence to a few days. Recall that we have used the relation between  $\tau$  and BH mass from Burke et al. (2021b) to generate the mock DRW light curves. We then use the CELERITE (Foreman-Mackey et al. 2017) package to infer  $\tau$  values from these light curves following the procedure of Burke et al. (2021b) using a maximum-likelihood fitting of a DRW Gaussian process to the light curve. Deviations from the DRW approximation may complicate the inference of a damping timescale. However, a more sophisticated analysis can be used to measure the damping timescales accurately (Stone et al. 2022). Our resulting recovered BH mass values from optical variability as a function of the input BH masses are shown in Figure 14 for sources that are significantly variable  $\sigma_{\text{var}} > 2$  with an input cadence of 25 days ( $g$ -band wide-fast-deep cadence), 3 days (wide-fast-deep cadence combining all bands), and a hybrid cadence described below.

Unsurprisingly, we find that we are unable to recover BH mass values below  $M_{\text{BH}} \sim 10^{6.4} M_{\odot}$  ( $M_{\text{BH}} \sim 10^{4.1} M_{\odot}$ ) given the limiting input cadence of 25 (3) days. Using the Burke et al. (2021b) relation, a  $\tau$  value of 25 days corresponds to  $M_{\text{BH}} \sim 10^5 M_{\odot}$  with a  $\sim 0.3$  dex scatter in the BH mass direction. However, such IMBHs can be identified in principle from their significant variability, and the cadence can be used as a rough upper-limit on the BH mass. We caution that other measures to select AGNs from the auto-correlation information are likely to miss AGNs with characteristic variability timescales less than the survey cadence, because such variability would be nearly indistinguishable from (uncorrelated) white noise. In order to test the feasibility of using a custom designed high-cadence mini-survey to identify IMBHs, we repeat the procedure

above using a rapid cadence of observations separated by 2.4 hours for 5 days but with daytime gaps, followed by the standard wide-fast-deep cadence. This hybrid cadence is able to recover the input BH mass values reasonably well, albeit with increased scatter. These relations are derived from a subset of the total AGN population, and the true dependence on other parameters like Eddington ratio as well as the exact cadence adopted.

## 4 DISCUSSION

### 4.1 Comparison with previous Work

#### 4.1.1 Variable fraction

We have constructed a mock sample consistent with the the PTF survey ( $R < 20.5$ ) to enable direct comparison with observed constraints on the optical variable fraction. We match the sample redshift distribution and survey parameters to observations (Baldassare et al. 2020). Our PTF-like model’s recovered variable fraction for all occupation fractions tested here is consistent with Baldassare et al. (2020) within  $2\sigma$  below  $M_{\star} \sim 10^9 M_{\odot}$ . The larger discrepancy at high stellar masses could perhaps be explained by larger contamination in the Baldassare et al. (2020) sample at these masses due to non-AGN variability or some form of incompleteness. For example, more massive AGNs with luminous blue/UV emission could be confused as lower mass star-forming galaxies, flattening out the observed variability fraction. Another obvious possibility is errors from assumptions or extrapolations of uncertain relations in our model. For example, the exact dependence of the derived variability amplitude on the AGN luminosity and accretion rate. Nevertheless, we consider this agreement to be excellent given the assumptions made in our model.

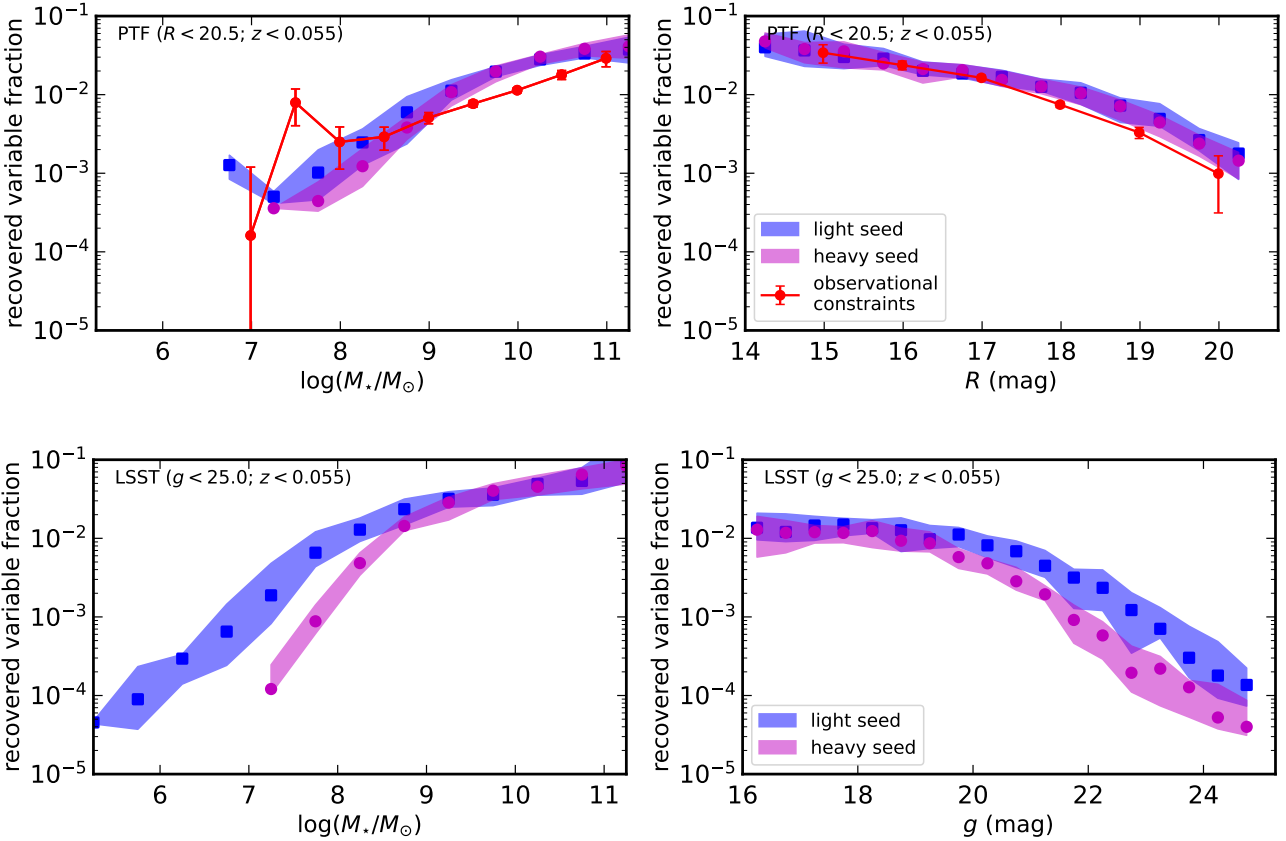


**Figure 11.** Recovered (observed) variable (defined as  $\sigma_{\text{var}} > 2$ ) AGN fraction versus host galaxy stellar mass (left) and aperture apparent magnitude (right) for the input “light” (blue/square symbols) and “heavy” (magenta/circle symbols) seeding scenarios for our PTF (upper panel) and LSST-like (lower panel) models. These recovered variable fractions are computed by selecting for variable light curves following mock observations as described in §3 after including all components of our demographics model as described in §2. The current observational constraints and  $1\sigma$  uncertainties from PTF are shown in red (Baldassare et al. 2020). We omit the data points in the most massive and faintest bins where the sample is highly incomplete for clarity. Our model results have greater statistical power at low stellar mass than the constraints from Baldassare et al. (2020) because that sample is limited to SDSS spectroscopically-targeted galaxies ( $r \lesssim 17.8$  mag), which is shallower than the PTF flux limit of  $R \sim 20.5$  mag.

#### 4.1.2 Active fraction

The active fraction—the fraction of galaxies radiating with Eddington luminosity ratio greater than  $\lambda_{\text{Edd,lim}}$ —can be defined as,

$$\lambda_{\mathcal{A}}(M_{\star}, \lambda_{\text{Edd,lim}}) = \lambda_{\text{occ}}(M_{\star}) \times \frac{\int_{\lambda_{\text{Edd,lim}}}^{\lambda_{\text{Edd,max}}} \xi(\lambda_{\text{Edd}}, \xi^*=1) d\lambda_{\text{Edd}}}{\int_{\lambda_{\text{Edd,min}}}^{\lambda_{\text{Edd,max}}} \xi(\lambda_{\text{Edd}}, \xi^*=1) d\lambda_{\text{Edd}}} \quad (17)$$

within the context of our model, where the ERDF  $\xi$  is given by Equation 6. Our definition differs slightly from the definitions adopted by other authors, who count any galaxy with an assigned  $\lambda_{\text{Edd}}$  value greater than  $\lambda_{\text{Edd,min}}$  toward the active fraction (e.g., Weigel et al. 2017). In this work, we have assigned each BH a  $\lambda_{\text{Edd}}$  value, but allow  $\lambda_{\text{Edd}}$  to be so small that the accretion activity effectively goes undetected.

A different approach was adopted by Pacucci et al. (2021), who developed an alternate theoretical model to predict the active fraction of dwarf AGNs. Their approach derives the active fraction from the number density and angular momentum content of the gas at the Bondi radius (as a proxy for the angular momentum content near an IMBH). After calibrating the model to observations, Pacucci et al.

(2021) find an active fraction  $\lambda_{\mathcal{A}} \propto (\log M_{\star})^{4.5}$  for  $10^7 M_{\odot} < M_{\star} < 10^{10} M_{\odot}$  for black holes accreting at  $\lambda_{\text{Edd}} \sim 0.1$ . These arguments imply that the observed optically-variable fraction is roughly the product of the optically unobscured fraction and the active fraction  $\lambda_{\text{var}} \sim (1 - f_{\text{obs}}) \times \lambda_{\mathcal{A}}$ .

In our model, we have assumed two mass-independent ERDFs for the blue/green (generally less massive, radiatively efficient accretion) and red (generally more massive, radiatively inefficient accretion) galaxy populations (Weigel et al. 2017). In contrast, the arguments from Pacucci et al. (2021) can be interpreted as a stellar mass dependent ERDF (also see Shankar et al. 2013; Hickox et al. 2014; Schulze et al. 2015; Bongiorno et al. 2016; Tucci & Volonteri 2017; Bernhard et al. 2018; Caplar et al. 2018) as opposed to a galaxy color/type dependent one. To test what impact these different assumptions have on the results, we re-run our forward Monte Carlo model, substituting a continuum of Eddington ratios given by an ERDF for an active fraction of the functional form  $\lambda_{\mathcal{A}} = 0.1 \times [\log(M_{\star}/M_{\odot})/9]^{4.5}$ , which closely matches the normalization in Figure 3 of Pacucci et al. (2021). Here, active galaxies are assumed to have  $\lambda_{\text{Edd}} = 0.1$  with a dispersion of 0.2 dex (typical for low- $z$  AGN samples; Pacucci et al. 2021; Greene & Ho 2007) and non-active galaxies have  $\lambda_{\text{Edd}} \approx 0$  as determined by random sampling. Our resulting detected variable

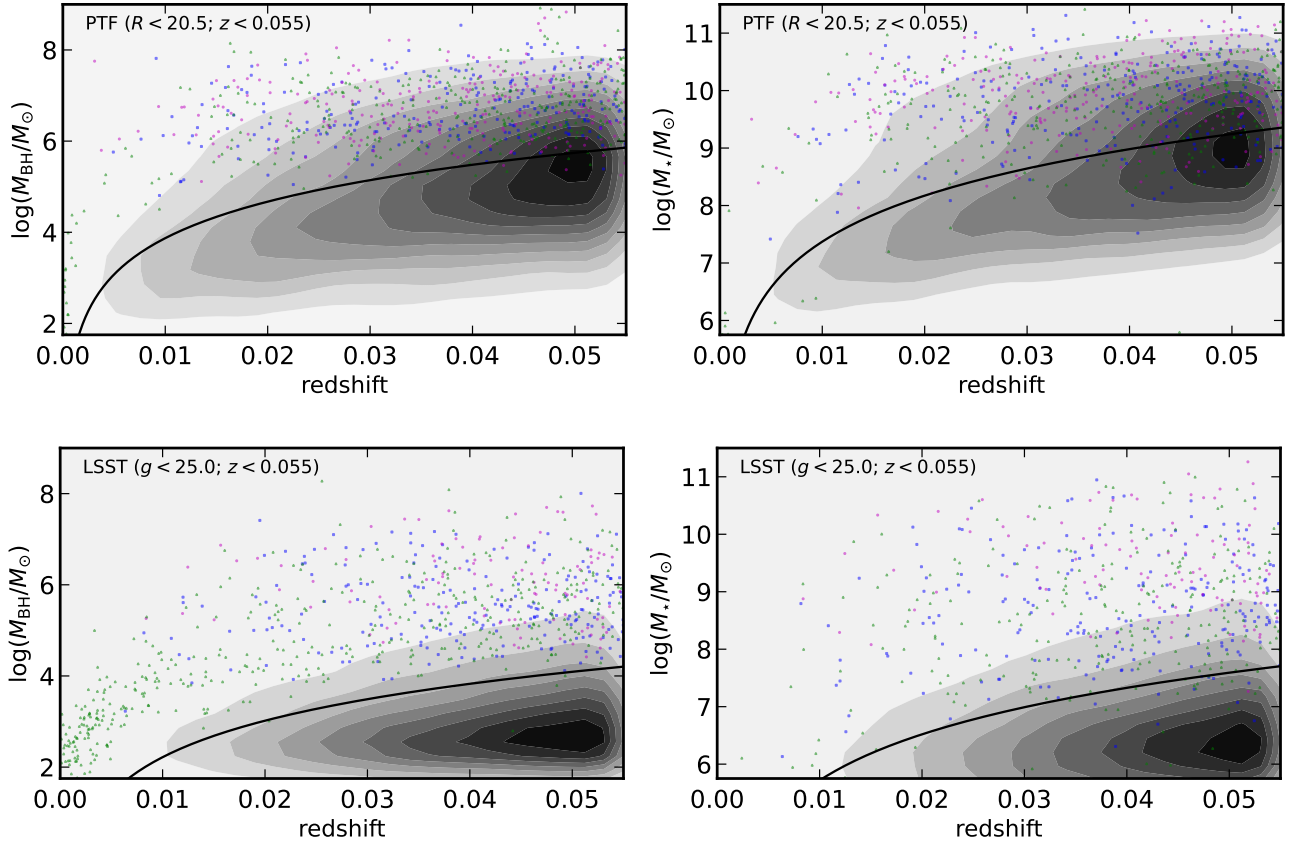


**Figure 12.** BH mass (left) and stellar mass (right) – redshift distributions for the input “light” (blue squares), “heavy” (magenta circles), and “light + wanderers” (green triangles) seeding scenarios for our PTF (upper panel) and LSST-like (lower panel) models. We assume measurement uncertainties of  $\sim 0.3$  dex in stellar mass. Darker contours represent denser regions of the distributions. The scatter points are recovered variable sources are computed by selecting for variable light curves following mock observations as described in §3 after including all components of our demographics model as described in §2. The gray-scale contours represents the underlying distribution of all sources (variable and non-variable) in each model. The solid black curves represents the theoretical mass detection limits following Appendix C assuming a typical rms variability amplitude of 0.1 mag. The distributions are from a single, representative bootstrap realization of our model results. The number of data points has been reduced by a factor of 10 (PTF) or 100 (LSST) to improve clarity.

fraction versus stellar mass for the PTF-like scenario is shown in Figure 15.

The resulting variable fraction has a very similar form as our model results. The computed variable fraction has a qualitatively similar scaling with magnitude and mass, which implies that the assumption of a mass-dependent ERDF does not strongly change the results, as expected if radiatively-efficient AGNs dominate the census. This is consistent with the findings of Weigel et al. (2017). Therefore, we can conclude that our results and the existing observational constraints are broadly consistent with an active fraction of the form  $\lambda_{\mathcal{A}} \propto (\log M_{\star})^{4.5}$  after calibration to the definition of “active” to the level of detectable accretion activity. This is reassuring and points to the fact that our model assumptions are reasonable. However, this simple Gaussian ERDF may not be consistent with the local AGN luminosity function.

#### 4.2 The effect of uncertainty on stellar mass measurements

The broad-band SED of galaxies can be used to infer the stellar mass of galaxies in large photo-metric catalogs. Uncertainties on these stellar masses are typically  $\sim 0.3$  dex and dominated by systematic uncertainties from model choices in stellar evolution (e.g.,

initial mass function, star formation history; Ciesla et al. 2015; Boquien et al. 2019). An additional problem is degeneracies between star-formation and AGN power-law emission. For example, Type 1 quasars with a blue/UV power-law continuum emission from the accretion disk (i.e., “big blue bump”) can be confused for dwarf starburst galaxies. This degeneracy can be more problematic when the redshift of the galaxy is uncertain or highly degenerate. Finally, variability from non-simultaneous observations can introduce additional errors in the SED. Because spectroscopic redshifts will not be available for every source in the large planned time-domain surveys, future work is needed to determine the strength of these degeneracies and how they can possibly be minimized (e.g., using the variability amplitude and timescale to independently constrain the strength of the AGN emission) over the entire range of stellar masses.

We then consider how uncertainties on stellar mass measurements affects the occupation function analysis in Figure 15, regardless of the exact sources of the uncertainty. To do this, we repeat the analysis of the variable fraction in Figure 15, which assumes a 0.3 dex uncertainty in stellar mass, using increasingly larger uncertainties of 0.6 and 0.9 dex in stellar mass. The results are shown in Appendix E. We have assumed a Gaussian distribution for the uncertainties, which may not be strictly true. We see that as the uncertainties increase, the

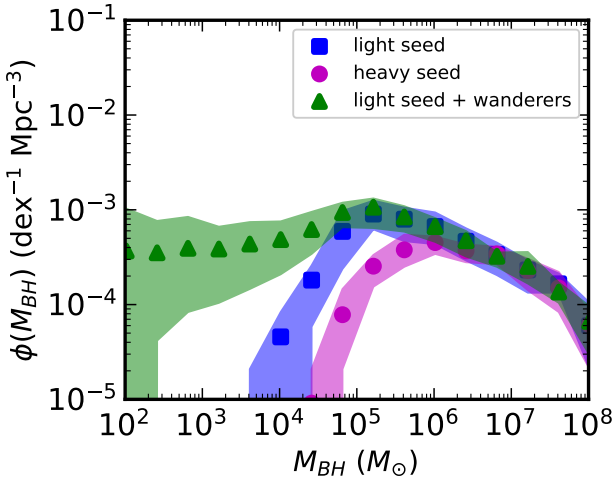


**Figure 13.** Recovered (observed) BH mass function for the input “light” (blue/square symbols), “heavy” (magenta/circle symbols), and “light + wanderers” (green triangle symbols) seeding scenarios for our LSST Rubin-like model. These recovered variable fractions are computed by selecting for variable light curves following mock observations as described in §3 after including all components of our demographics model as described in §2.

variable fraction “flattens out” as the stellar masses are smeared into adjacent bins and would result in a larger number of false positive IMBH candidates.

#### 4.3 Recovery of the host galaxy-black hole mass scaling relation

We show the recovered  $M_{BH} - M_{\star}$  relation for variability-selected sources to investigate the influence of variability selection effects in Figure 16. The more massive and luminous black holes tend to have larger observed variability amplitudes at fixed stellar mass due to having less host galaxy dilution (see discussion in §2.7). See Lauer et al. (2007) for a related selection bias. We find that this bias results in variability-selected  $M_{BH}$  values that are on average larger by  $\sim 1$  dex than expected from the Reines & Volonteri (2015) relation for  $M_{\star} < 10^9 M_{\odot}$  host galaxies. This bias is only slightly reduced with more photo-metrically sensitive light curves. We therefore expect variability-selected IMBH candidates in dwarf galaxies to be strongly affected by this bias. This demonstrates the importance of obtaining additional  $M_{BH}$  estimates for variability-selected AGNs, such as from the variability timescale (Burke et al. 2021c) or broad emission line signatures (Shen 2013), rather than using the stellar mass alone as a proxy.

#### 4.4 Extension beyond the local Universe

We have shown that the number of detectable IMBHs falls off quickly with redshift (Figure 12) faster than the gain in volume. However, extensions of our model beyond the local Universe are straightforward if one is interested in AGNs with somewhat larger BH masses,  $M_{BH} \sim 10^5 - 10^6 M_{\odot}$ , that are detectable at intermediate redshifts (e.g., Guo et al. 2020a; Burke et al. 2021a). To extend the treatment to higher redshifts, one could adopt the same GSMF form of Equation 1, but adjust the parameters based on the redshift range using observational constraints on the GSMF evolution (e.g., Marchesini

et al. 2009; Adams et al. 2021). A model for the commensurate host-galaxy  $K$ -correction (e.g., Chilingarian et al. 2010) to the mass-to-light ratios would need to be considered. At intermediate redshifts, the host galaxy-BH mass relation may have a different normalization and slope that better describes the AGN population (e.g., Caplar et al. 2018; Ding et al. 2020). Obviously, the GSMF in the dwarf galaxy regime becomes less well-constrained with increasing redshift. In addition, whether and how the ERDF of the obscured AGN fraction changes with redshift is uncertain at present. Finally, there are other factors (e.g., dwarf galaxy-galaxy mergers) that complicate using occupation fraction as a direct tracer of seeding scenarios at high redshift (Volonteri 2010; Ricarte & Natarajan 2018; Mezcua et al. 2019; Buchner et al. 2019). Investigations of IMBH evolution in dwarf galaxies using cosmological simulations that incorporate the relevant physics on these scales may help illuminate the properties of the evolving IMBH population (Sharma et al. 2022; Haidar et al. 2022).

#### 4.5 Caveats & Future work

Our methodology can be extended and applied to other wavelengths, such as sensitive X-ray observations of dwarf galaxies with eROSITA (Predehl et al. 2021; Latimer et al. 2021) or time-domain UV imaging surveys (Sagiv et al. 2014; Kulkarni et al. 2021). Better constraints on the shape and normalization of the ERDF in the IMBH regime would help us compute our forecasts for the total number of detectable variable dwarf AGNs. Ultimately, a variety of multi-wavelength probes are desired to derive robust constraints on the occupation fraction.

Though counter-intuitive, it has been amply demonstrated by many previous workers including Ricarte & Natarajan (2018) that local observations of the occupation fraction of black holes in low mass dwarf galaxies could serve to discriminate between high redshift initial seeding models. Despite the modulation of black growth by accretion over cosmic time from early seeds, the memory of these initial conditions survives in particular for these low mass galaxy hosts that preferentially host IMBHs. And while current observations do not offer conclusive evidence, the prospects for doing so are promising as we describe below.

Our modeling indicates that the “light” seeding scenario is slightly more consistent with current observational constraints from dwarf AGN variability, however, the current observational constraints in the dwarf galaxy regime (Figure 11) are not particularly strong. The discriminating power of optical variability to distinguish between seeding scenarios lies in the capability to accurately measure the variable detected fraction in  $M_{\star} \lesssim 10^8 M_{\odot}$  galaxies. Our model predictions for the occupation fractions in scenario (i) and (ii) can be differentiated at the  $2 - 3\sigma$  level in the detectable variable fraction at  $M_{\star} \lesssim 10^8 M_{\odot}$  (see Figure 11). Therefore, we are unable to strongly rule-out either seeding scenario (or a mixture of several) at this time except for ones that predict occupation fractions of zero in dwarf galaxies. The large uncertainties here are dominated by uncertainties in the GSMF, optical variability properties, and scatter in the host-mass scaling relation. We expect constraints on some of these quantities to improve dramatically in the near future.

We have made some assumptions in our model using the average properties of the galaxy population to predict variability amplitudes. For example, the predicted observed variability amplitudes in our model depend on our population-level model of host galaxy color index and the level of contamination in the light curve aperture. In order to eliminate these assumptions, one could directly use catalog properties, e.g. measured host galaxy luminosities within light curve apertures, from the parent sample of the observations as long as one

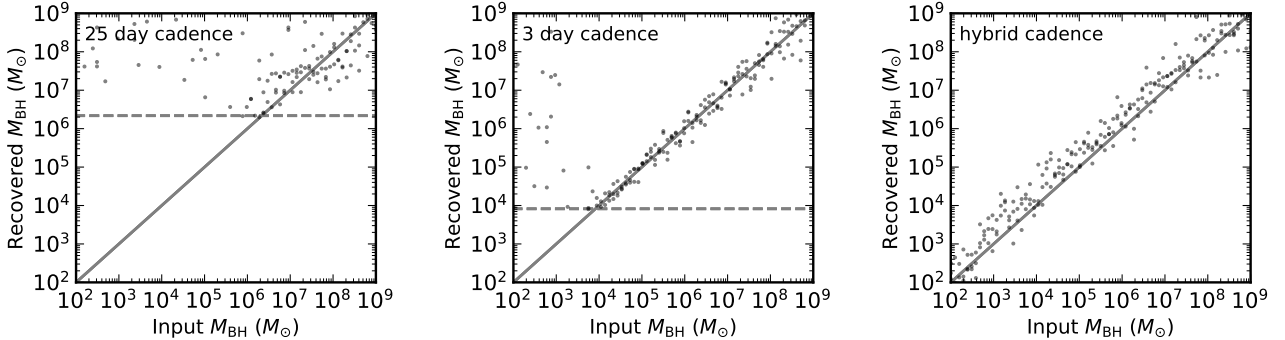


**Figure 14.** Recovered BH mass versus input BH mass for using mock light curves for various cadences scenarios of 3 days, 25 days, and a hybrid cadence of 25 days plus a  $\sim$ hourly cadence for 5 days assuming the BH mass–damping timescale relation of Burke et al. (2021b). The horizontal dashed gray line represents the BH mass with variability timescale equal to the limiting cadence of the light curves. The  $y = x$  line is shown as a gray solid line. The hybrid cadence provides the best recovery of IMBH masses measured from realistic light curves of the three cadence modes.

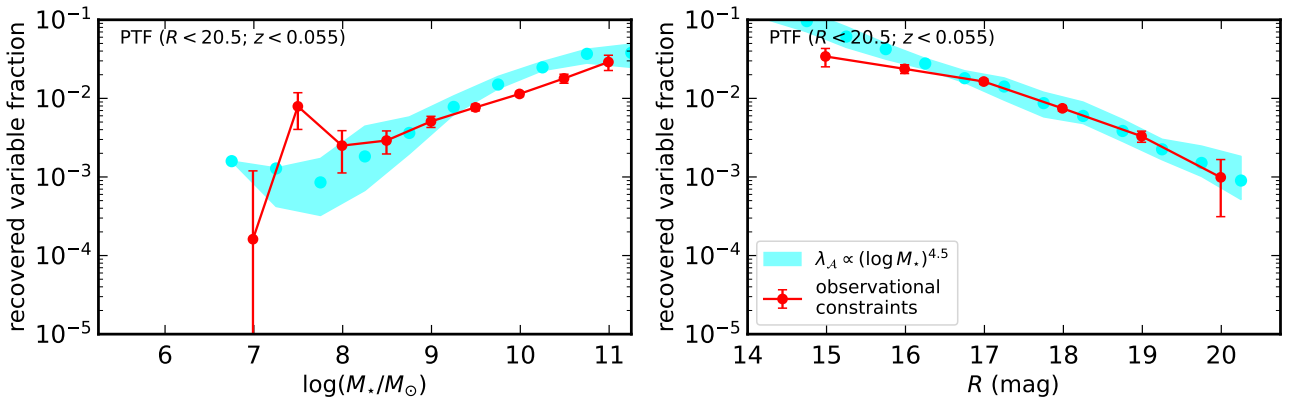


**Figure 15.** Recovered (observed) variable AGN fraction in bins of stellar mass (left) and aperture apparent magnitude (right) for the active fraction prediction from Pacucci et al. (2021) (cyan/square symbols) for our PTF-like model. An active fraction of the form  $\lambda_{\mathcal{A}} \propto (\log M_{\star})^{4.5}$  is very similar shape to our model results in Figure 11 and is a reasonable match to the observational constraints. These recovered variable fractions are computed by selecting for variable light curves following mock observations as described in §3 after including all components of our demographics model as described in §2. The current observational constraints and  $1\sigma$  uncertainties from PTF are shown in red (Baldassare et al. 2020). We omit the data points in the most massive and faintest bins where the sample is highly incomplete for clarity.

is cautious about the relevant selection biases in the parent sample properties. Additionally, we caution that the MacLeod et al. (2010); Suberlak et al. (2021); Burke et al. (2021b) parameters are likely to be affected by selection biases, and whether these these relations hold in the ADAF/RIAF regime is also somewhat uncertain.

Nevertheless, we have demonstrated the expected capabilities and prospects of the LSST Rubin wide-fast-deep survey for IMBH identification via optical variability. With robust observational constraints, the problem could be turned around to become an inference problem to constrain the multiple free parameters in our model with priors derived from observational constraints (Caplar et al. 2015; Weigel et al. 2017). Improved constraints on the optical variability properties in the IMBH regime will further reduce the uncertainties. Additionally, a wide-field, deep, flux limited catalog of stellar masses of low-redshift galaxies is urgently needed in the Southern Hemisphere to obtain enough statistical power to distinguish between seeding mechanisms with LSST Rubin.

#### 4.6 A note on the optical variability amplitude

The arguments in §2.7 could pose a quantifiable, unified interpretation of the nuclear optical variability amplitude of galaxies and AGNs where the intrinsic variability amplitude is set by the accretion rate and BH mass, but the resulting observed variability amplitude is diluted by the host galaxy emission. This approach provides quantitative phenomenological predictions for IMBH optical variability, which is argued to show fast and small amplitude variability (e.g., Martínez-Palomera et al. 2020).

## 5 CONCLUSIONS

We have investigated prospects for IMBH discovery using optical variability with LSST Rubin by building a forward Monte Carlo model beginning from the galaxy stellar mass function. After assuming several possibilities for the BH occupation fraction, and incorporating observed galaxy-BH scaling relations, we demonstrate

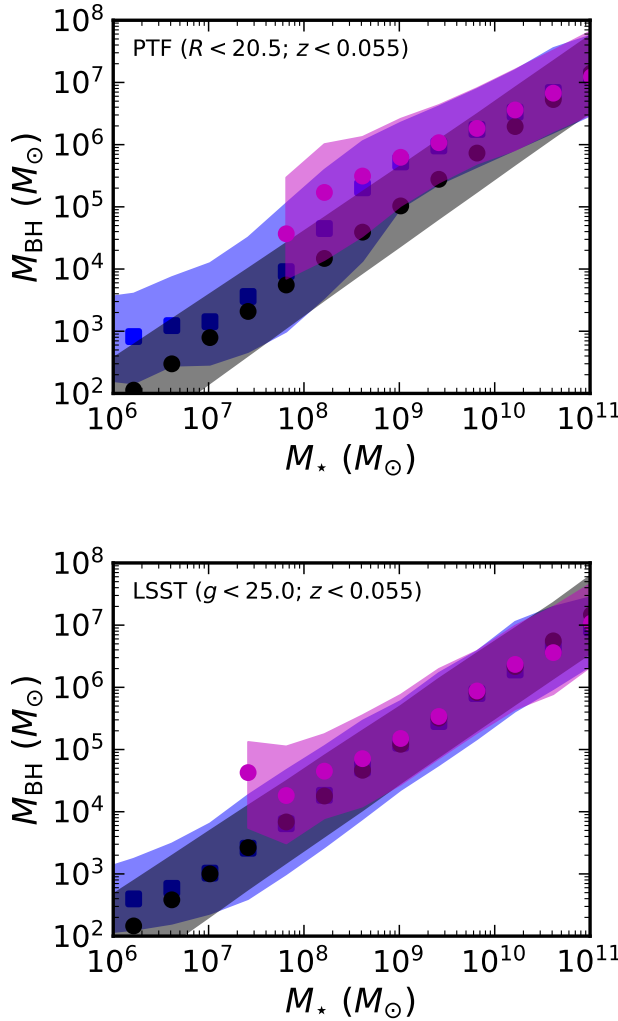


**Figure 16.** Recovered  $M_{\text{BH}} - M_{\star}$  relation for variability-selected sources for the “heavy” and “light” seeding scenarios (strongly overlapping) compared to the input relation given by Reines & Volonteri (2015) (gray) for PTF (upper panel) and LSST-like (lower panel) models.

our model’s capability to reproduce existing observations. Below, we summarize our main conclusions:

- (i) We confirm the discriminating power of optical variability to distinguish between BH occupation fractions by accurately measuring the variable detected fraction in the  $M_{\star} \sim 10^6 - 10^8 M_{\odot}$  regime.
- (ii) Current observational constraints are however, insufficient to constrain early seeding scenarios given their limited statistical power and the theoretical uncertainties in this regime. However, they are inconsistent with an IMBH occupation fraction of zero near  $M_{\star} \sim 10^8 M_{\odot}$ .
- (iii) We demonstrate the resulting BH masses may be biased toward larger  $M_{\text{BH}}$  on average at fixed  $M_{\star}$  from an Eddington-type bias, depending on the photometric precision of the survey.
- (iv) Given these findings, we forecast detection of up to  $\sim 10^2$  IMBHs with LSST Rubin using optical variability assuming an optimistic “light” seeding scenario and perhaps more if there exists a

population of wandering IMBHs with an Eddington ratio distribution similar to that of SMBHs in red galaxies.

(v) A targeted  $\sim$  hourly cadence program over a few nights can provide constraints on the BH masses of IMBHs given their expected rapid variability timescales.

## ACKNOWLEDGEMENTS

We thank Chris Done and Rodrigo Nemmen for helpful discussions. We thank Konstantin Malanchev and Qifeng Cheng for referring us to an improved algorithm for generating DRW time series. CJB acknowledges support from the Illinois Graduate Survey Science Fellowship. YS acknowledges support from NSF grant AST-2009947. XL and ZFW acknowledge support from the University of Illinois Campus Research Board and NSF grant AST-2108162. PN gratefully acknowledges support at the Black Hole Initiative (BHI) at Harvard as an external PI with grants from the Gordon and Betty Moore Foundation and the John Templeton Foundation. This research was supported in part by the National Science Foundation under Grant No. NSF PHY-1748958. This research made use of Astropy,<sup>7</sup> a community-developed core Python package for Astronomy (Astropy Collaboration et al. 2018).

## DATA AVAILABILITY

The data used in this work is available following the references and URLs in the text. Our pre-computed SED templates are available at <https://doi.org/10.5281/zenodo.6812008>.

## REFERENCES

- Abbott R., et al., 2021, *ApJ*, **913**, L7
- Abel T., Bryan G. L., Norman M. L., 2002, *Science*, **295**, 93
- Adams N. J., Bowler R. A. A., Jarvis M. J., Häußler B., Lagos C. D. P., 2021, *MNRAS*, **506**, 4933
- Agostino C. J., Salim S., 2019, *ApJ*, **876**, 12
- Aird J., Coil A. L., Georgakakis A., Nandra K., Barro G., Pérez-González P. G., 2015, *MNRAS*, **451**, 1892
- Ajello M., Alexander D. M., Greiner J., Madejski G. M., Gehrels N., Burlon D., 2012, *ApJ*, **749**, 21
- Alexander T., Natarajan P., 2014, *Science*, **345**, 1330
- Ananna T. T., et al., 2022, arXiv e-prints, [p. arXiv:2201.05603](https://arxiv.org/abs/2201.05603)
- Anastasopoulou K., Zezas A., Steiner J. F., Reig P., 2022, *MNRAS*,
- Andrews S. K., Driver S. P., Davies L. J. M., Kafle P. R., Robotham A. S. G., Wright A. H., 2017, *MNRAS*, **464**, 1569
- Antonini F., Barausse E., Silk J., 2015, *ApJ*, **812**, 72
- Antonini F., Gieles M., Gualandris A., 2019, *MNRAS*, **486**, 5008
- Arnaud K. A., 1996, in Jacoby G. H., Barnes J., eds, Astronomical Society of the Pacific Conference Series Vol. 101, Astronomical Data Analysis Software and Systems V. p. 17
- Astropy Collaboration et al., 2018, *AJ*, **156**, 123
- Bañados E., et al., 2018, *Nature*, **553**, 473
- Baganoff F. K., et al., 2003, *ApJ*, **591**, 891
- Baldassare V. F., Reines A. E., Gallo E., Greene J. E., 2015, *ApJ*, **809**, L14
- Baldassare V. F., et al., 2016, *ApJ*, **829**, 57
- Baldassare V. F., Geha M., Greene J., 2018, *ApJ*, **868**, 152
- Baldassare V. F., Geha M., Greene J., 2020, *ApJ*, **896**, 10
- Baldry I. K., Glazebrook K., Brinkmann J., Ivezić Ž., Lupton R. H., Nichol R. C., Szalay A. S., 2004, *ApJ*, **600**, 681
- Baldry I. K., et al., 2012, *MNRAS*, **421**, 621

<sup>7</sup> <http://www.astropy.org>

Baldwin J. A., Phillips M. M., Terlevich R., 1981, *PASP*, **93**, 5

Barth A. J., Ho L. C., Rutledge R. E., Sargent W. L. W., 2004, *ApJ*, **607**, 90

Barth A. J., Voevodkin A., Carson D. J., Woźniak P., 2014, *AJ*, **147**, 12

Baxter E. J., Croon D., McDermott S. D., Sakstein J., 2021, *ApJ*, **916**, L16

Begelman M. C., Volonteri M., Rees M. J., 2006, *MNRAS*, **370**, 289

Bell E. F., McIntosh D. H., Katz N., Weinberg M. D., 2003, *ApJS*, **149**, 289

Bellm E. C., et al., 2019, *PASP*, **131**, 018002

Bellovary J. M., Governato F., Quinn T. R., Wadsley J., Shen S., Volonteri M., 2010, *ApJ*, **721**, L148

Bellovary J. M., Cleary C. E., Munshi F., Tremmel M., Christensen C. R., Brooks A., Quinn T. R., 2019, *MNRAS*, **482**, 2913

Bernhard E., Mullaney J. R., Aird J., Hickox R. C., Jones M. L., Stanley F., Grimmett L. P., Daddi E., 2018, *MNRAS*, **476**, 436

Blanton M. R., Kazin E., Muna D., Weaver B. A., Price-Whelan A., 2011, *AJ*, **142**, 31

Blanton M. R., et al., 2017, *AJ*, **154**, 28

Blecha L., Cox T. J., Loeb A., Hernquist L., 2011, *MNRAS*, **412**, 2154

Blecha L., et al., 2016, *MNRAS*, **456**, 961

Bond J. R., Arnett W. D., Carr B. J., 1984, *ApJ*, **280**, 825

Bongiorno A., et al., 2016, *A&A*, **588**, A78

Boquien M., Burgarella D., Roehlly Y., Buat V., Ciesla L., Corre D., Inoue A. K., Salas H., 2019, *A&A*, **622**, A103

Bromm V., Loeb A., 2003, *ApJ*, **596**, 34

Buchner J., Treister E., Bauer F. E., Sartori L. F., Schawinski K., 2019, *ApJ*, **874**, 117

Burke C. J., Shen Y., Chen Y.-C., Scaringi S., Faucher-Giguere C.-A., Liu X., Yang Q., 2020, *ApJ*, **899**, 136

Burke C. J., et al., 2021a, arXiv e-prints, p. arXiv:2111.03079

Burke C. J., et al., 2021b, *Science*, **373**, 789

Burke C. J., Liu X., Chen Y.-C., Shen Y., Guo H., 2021c, *MNRAS*, **504**, 543

Butler N. R., Bloom J. S., 2011, *AJ*, **141**, 93

Cann J. M., Satyapal S., Abel N. P., Ricci C., Secrest N. J., Blecha L., Gliozzi M., 2018, *ApJ*, **861**, 142

Caplar N., Lilly S. J., Trakhtenbrot B., 2015, *ApJ*, **811**, 148

Caplar N., Lilly S. J., Trakhtenbrot B., 2017, *ApJ*, **834**, 111

Caplar N., Lilly S. J., Trakhtenbrot B., 2018, *ApJ*, **867**, 148

Carlson M. N., Holtzman J. A., 2001, *PASP*, **113**, 1522

Chakravorty S., Elvis M., Ferland G., 2014, *MNRAS*, **437**, 740

Chilingarian I. V., Melchior A.-L., Zolotukhin I. Y., 2010, *MNRAS*, **405**, 1409

Chilingarian I. V., Katkov I. Y., Zolotukhin I. Y., Grishin K. A., Beletsky Y., Boutsia K., Osip D. J., 2018, *ApJ*, **863**, 1

Choi Y., Gibson R. R., Becker A. C., Ivezić Ž., Connolly A. J., MacLeod C. L., Ruan J. J., Anderson S. F., 2014, *ApJ*, **782**, 37

Ciesla L., et al., 2015, *A&A*, **576**, A10

Civano F., et al., 2012, *ApJS*, **201**, 30

Davies M. B., Miller M. C., Bellovary J. M., 2011, *ApJ*, **740**, L42

Devecchi B., Volonteri M., 2009, *ApJ*, **694**, 302

Devecchi B., Volonteri M., Colpi M., Haardt F., 2010, *MNRAS*, **409**, 1057

Ding X., et al., 2020, *ApJ*, **888**, 37

Done C., Davis S. W., Jin C., Blaes O., Ward M., 2012, *MNRAS*, **420**, 1848

Driver S. P., et al., 2011, *MNRAS*, **413**, 971

Duras F., et al., 2020, *A&A*, **636**, A73

Eracleous M., Hwang J. A., Flohic H. M. L. G., 2010, *ApJS*, **187**, 135

Fabian A. C., Rees M. J., 1995, *MNRAS*, **277**, L55

Fan X., et al., 2001, *AJ*, **122**, 2833

Farrell S. A., Webb N. A., Barret D., Godet O., Rodrigues J. M., 2009, *Nature*, **460**, 73

Farrell S. A., et al., 2014, *MNRAS*, **437**, 1208

Feng H., Soria R., 2011, *New Astron. Rev.*, **55**, 166

Filippenko A. V., Ho L. C., 2003, *ApJ*, **588**, L13

Fiore F., et al., 2012, *A&A*, **537**, A16

Foreman-Mackey D., Agol E., Ambikasaran S., Angus R., 2017, *AJ*, **154**, 220

Fragione G., Silk J., 2020, *MNRAS*, **498**, 4591

Fragione G., Ginsburg I., Kocsis B., 2018, *ApJ*, **856**, 92

Fryer C. L., Woosley S. E., Heger A., 2001, *ApJ*, **550**, 372

Gallo E., Sesana A., 2019, *ApJ*, **883**, L18

Genzel R., Eisenhauer F., Gillessen S., 2010, *Reviews of Modern Physics*, **82**, 3121

Gierliński M., Done C., Page K., 2009, *MNRAS*, **392**, 1106

Graham A. W., 2020, *MNRAS*, **492**, 3263

Greene J. E., 2012, *Nature Communications*, **3**, 1304

Greene J. E., Ho L. C., 2007, *ApJ*, **670**, 92

Greene J. E., Strader J., Ho L. C., 2020, *ARA&A*, **58**, 257

Grimm H. J., Gilfanov M., Sunyaev R., 2003, *MNRAS*, **339**, 793

Groves B. A., Heckman T. M., Kauffmann G., 2006, *MNRAS*, **371**, 1559

Guo H., et al., 2020a, *MNRAS*, **496**, 3636

Guo M., Inayoshi K., Michiyama T., Ho L. C., 2020b, *ApJ*, **901**, 39

Gürkan M. A., Freitag M., Rasio F. A., 2004, *ApJ*, **604**, 632

Haehnelt M. G., Rees M. J., 1993, *MNRAS*, **263**, 168

Haidar H., et al., 2022, arXiv e-prints, p. arXiv:2201.09888

Hao L., et al., 2005, *AJ*, **129**, 1795

Hickox R. C., Mullaney J. R., Alexander D. M., Chen C.-T. J., Civano F. M., Goulingd A. D., Hainline K. N., 2014, *ApJ*, **782**, 9

Ho L. C., 2009, *ApJ*, **699**, 626

Holley-Bockelmann K., Gültekin K., Shoemaker D., Yunes N., 2008, *ApJ*, **686**, 829

Inayoshi K., Visbal E., Haiman Z., 2020, *ARA&A*, **58**, 27

Ivezić Ž., et al., 2019, *ApJ*, **873**, 111

Jones M. L., Hickox R. C., Black C. S., Hainline K. N., DiPompeo M. A., Goulingd A. D., 2016, *ApJ*, **826**, 12

Kaaret P., Feng H., Roberts T. P., 2017, *ARA&A*, **55**, 303

Kauffmann G., Heckman T. M., 2009, *MNRAS*, **397**, 135

Kelly B. C., Bechtold J., Siemiginowska A., 2009, *ApJ*, **698**, 895

Koushiappas S. M., Bullock J. S., Dekel A., 2004, *MNRAS*, **354**, 292

Kozłowski S., 2016, *ApJ*, **826**, 118

Kroupa P., Subr L., Jerabkova T., Wang L., 2020, *MNRAS*, **498**, 5652

Kulkarni S. R., et al., 2021, arXiv e-prints, p. arXiv:2111.15608

LIGO Scientific Collaboration Virgo Collaboration 2020, *Phys. Rev. Lett.*, **125**, 101102

Laor A., Netzer H., 1989, *MNRAS*, **238**, 897

Latimer C. J., Reines A. E., Bogdan A., Kraft R., 2021, arXiv e-prints, p. arXiv:2111.10388

Lauer T. R., Tremaine S., Richstone D., Faber S. M., 2007, *ApJ*, **670**, 249

Law N. M., et al., 2009, *PASP*, **121**, 1395

Lehmer B. D., et al., 2020, *ApJS*, **248**, 31

Leigh N. W. C., Lützgendorf N., Geller A. M., Maccarone T. J., Heinke C., Sesana A., 2014, *MNRAS*, **444**, 29

Lin D., et al., 2018, *Nature Astronomy*, **2**, 656

Liske J., et al., 2015, *MNRAS*, **452**, 2087

Liu H.-Y., Yuan W., Dong X.-B., Zhou H., Liu W.-J., 2018, *ApJS*, **235**, 40

Lodato G., Natarajan P., 2006, *MNRAS*, **371**, 1813

Lodato G., Natarajan P., 2007, *MNRAS*, **377**, L64

Loeb A., Rasio F. A., 1994, *ApJ*, **432**, 52

Luo B., et al., 2017, *ApJS*, **228**, 2

Lupi A., Colpi M., Devecchi B., Galanti G., Volonteri M., 2014, *MNRAS*, **442**, 3616

Ma L., Hopkins P. F., Ma X., Anglés-Alcázar D., Faucher-Giguère C.-A., Kelley L. Z., 2021, *MNRAS*, **508**, 1973

MacLeod C. L., et al., 2010, *ApJ*, **721**, 1014

Madau P., Rees M. J., 2001, *ApJ*, **551**, L27

Magorrian J., et al., 1998, *AJ*, **115**, 2285

Makishima K., Maejima Y., Mitsuda K., Bradt H. V., Remillard R. A., Tuohy I. R., Hoshi R., Nakagawa M., 1986, *ApJ*, **308**, 635

Marchesini D., van Dokkum P. G., Förster Schreiber N. M., Franx M., Labbé I., Wuyts S., 2009, *ApJ*, **701**, 1765

Martin D. C., et al., 2005, *ApJ*, **619**, L1

Martínez-Palomera J., Lira P., Bhalla-Ladd I., Förster F., Plotkin R. M., 2020, *ApJ*, **889**, 113

Matsuoka Y., Strauss M. A., Price Ted N. I., DiDonato M. S., 2014, *ApJ*, **780**, 162

McHardy I. M., Koerding E., Knigge C., Uttley P., Fender R. P., 2006, *Nature*, **444**, 730

Merloni A., et al., 2014, *MNRAS*, **437**, 3550

Mezcua M., 2019, *Nature Astronomy*, **3**, 6

Mezcua M., Domínguez Sánchez H., 2020, *ApJ*, **898**, L30

Mezcua M., Roberts T. P., Lobanov A. P., Sutton A. D., 2015, *MNRAS*, **448**, 1893

Mezcua M., Civano F., Fabbiano G., Miyaji T., Marchesi S., 2016, *ApJ*, **817**, 20

Mezcua M., Suh H., Civano F., 2019, *MNRAS*, **488**, 685

Miller M. C., Hamilton D. P., 2002, *MNRAS*, **330**, 232

Miller B. P., Gallo E., Greene J. E., Kelly B. C., Treu T., Woo J.-H., Baldassare V., 2015, *ApJ*, **799**, 98

Mitsuda K., et al., 1984, *PASJ*, **36**, 741

Molina M., Eracleous M., Barth A. J., Maoz D., Runnoe J. C., Ho L. C., Shields J. C., Walsh J. L., 2018, *ApJ*, **864**, 90

Moran E. C., Filippenko A. V., Ho L. C., Shields J. C., Belloni T., Comastri A., Snowden S. L., Sramek R. A., 1999, *PASP*, **111**, 801

Narayan R., Yi I., 1994, *ApJ*, **428**, L13

Narayan R., Yi I., 1995, *ApJ*, **452**, 710

Narayan R., Mahadevan R., Grindlay J. E., Popham R. G., Gammie C., 1998, *ApJ*, **492**, 554

Natarajan P., 2014, *General Relativity and Gravitation*, **46**, 1702

Natarajan P., 2021, *MNRAS*, **501**, 1413

Nemmen R. S., Storchi-Bergmann T., Eracleous M., 2014, *MNRAS*, **438**, 2804

O’Leary R. M., Loeb A., 2009, *MNRAS*, **395**, 781

Ofek E. O., et al., 2012, *PASP*, **124**, 62

Pacucci F., Mezcua M., Regan J. A., 2021, arXiv e-prints, p. [arXiv:2107.09069](https://arxiv.org/abs/2107.09069)

Pedregosa F., et al., 2011, *Journal of Machine Learning Research*, **12**, 2825

Pesce D. W., et al., 2021, *ApJ*, **923**, 260

Portegies Zwart S. F., McMillan S. L. W., 2002, *ApJ*, **576**, 899

Portegies Zwart S. F., Baumgardt H., Hut P., Makino J., McMillan S. L. W., 2004, *Nature*, **428**, 724

Predehl P., et al., 2021, *A&A*, **647**, A1

Reines A. E., Volonteri M., 2015, *ApJ*, **813**, 82

Reines A. E., Greene J. E., Geha M., 2013, *ApJ*, **775**, 116

Reines A. E., Condon J. J., Darling J., Greene J. E., 2020, *ApJ*, **888**, 36

Ricarte A., Natarajan P., 2018, *MNRAS*, **481**, 3278

Ricarte A., Tremmel M., Natarajan P., Zimmer C., Quinn T., 2021a, *MNRAS*, **503**, 6098

Ricarte A., Tremmel M., Natarajan P., Quinn T., 2021b, *ApJ*, **916**, L18

Richards G. T., et al., 2006, *ApJS*, **166**, 470

Rizzuto F. P., et al., 2021, *MNRAS*, **501**, 5257

Rumbaugh N., et al., 2018, *ApJ*, **854**, 160

Sagiv I., et al., 2014, *AJ*, **147**, 79

Sánchez J., et al., 2020, *MNRAS*, **497**, 210

Sartori L. F., Schawinski K., Treister E., Trakhtenbrot B., Koss M., Shirazi M., Oh K., 2015, *MNRAS*, **454**, 3722

Sartori L. F., Trakhtenbrot B., Schawinski K., Caplar N., Treister E., Zhang C., 2019, *ApJ*, **883**, 139

Scaringi S., et al., 2015, *Science Advances*, **1**, e1500686

Schechter P., 1976, *ApJ*, **203**, 297

Schulze A., Wisotzki L., Husemann B., 2009, *A&A*, **507**, 781

Schulze A., et al., 2015, *MNRAS*, **447**, 2085

Scoville N., et al., 2007, *ApJS*, **172**, 1

Seepaul B., Pacucci F., Narayan R., 2022, arXiv e-prints, p. [arXiv:2204.12498](https://arxiv.org/abs/2204.12498)

Servillat M., Farrell S. A., Lin D., Godet O., Barret D., Webb N. A., 2011, *ApJ*, **743**, 6

Shakura N. I., Sunyaev R. A., 1973, *A&A*, **500**, 33

Shankar F., Weinberg D. H., Miralda-Escudé J., 2013, *MNRAS*, **428**, 421

Sharma R. S., Brooks A. M., Tremmel M., Bellovary J., Ricarte A., Quinn T. R., 2022, arXiv e-prints, p. [arXiv:2203.05580](https://arxiv.org/abs/2203.05580)

Shen Y., 2013, *Bulletin of the Astronomical Society of India*, **41**, 61

Shen Y., et al., 2009, *ApJ*, **697**, 1656

Sicilia A., et al., 2022, *ApJ*, **924**, 56

Simm T., Salvato M., Saglia R., Ponti G., Lanzuisi G., Trakhtenbrot B., Nandra K., Bender R., 2016, *A&A*, **585**, A129

Stone N. C., Küpper A. H. W., Ostriker J. P., 2017, *MNRAS*, **467**, 4180

Stone Z., et al., 2022, arXiv e-prints, p. [arXiv:2201.02762](https://arxiv.org/abs/2201.02762)

Suberlak K. L., Ivezic Ž., MacLeod C., 2021, *ApJ*, **907**, 96

Taylor E. N., et al., 2015, *MNRAS*, **446**, 2144

Trump J. R., et al., 2015, *ApJ*, **811**, 26

Tucci M., Volonteri M., 2017, *A&A*, **600**, A64

Veilleux S., Osterbrock D. E., 1987, *ApJS*, **63**, 295

Volonteri M., 2010, *A&ARv*, **18**, 279

Volonteri M., Perna R., 2005, *MNRAS*, **358**, 913

Volonteri M., Haardt F., Madau P., 2003, *ApJ*, **582**, 559

Volonteri M., Lodato G., Natarajan P., 2008, *MNRAS*, **383**, 1079

Wang F., et al., 2021, *ApJ*, **907**, L1

Ward C., et al., 2020, arXiv e-prints, p. [arXiv:2011.11656](https://arxiv.org/abs/2011.11656)

Ward C., et al., 2021, arXiv e-prints, p. [arXiv:2110.13098](https://arxiv.org/abs/2110.13098)

Weigel A. K., Schawinski K., Bruderer C., 2016, *MNRAS*, **459**, 2150

Weigel A. K., Schawinski K., Caplar N., Wong O. I., Treister E., Trakhtenbrot B., 2017, *ApJ*, **845**, 134

Wilhite B. C., Brunner R. J., Grier C. J., Schneider D. P., vanden Berk D. E., 2008, *MNRAS*, **383**, 1232

Wolter A., Fruscione A., Mapelli M., 2018, *ApJ*, **863**, 43

Wright A. H., et al., 2017, *MNRAS*, **470**, 283

Wu X.-B., et al., 2015, *Nature*, **518**, 512

Xue Y. Q., 2017, *New Astron. Rev.*, **79**, 59

Young M., et al., 2012, *ApJ*, **748**, 124

Yuan F., Quataert E., Narayan R., 2003, *ApJ*, **598**, 301

Yuan F., Cui W., Narayan R., 2005, *ApJ*, **620**, 905

Yuan F., Zdziarski A. A., Xue Y., Wu X.-B., 2007, *ApJ*, **659**, 541

Zibetti S., Charlot S., Rix H.-W., 2009, *MNRAS*, **400**, 1181

Zinnecker H., Keable C. J., Dunlop J. S., Cannon R. D., Griffiths W. K., 1988, in Grindlay J. E., Philip A. G. D., eds, Vol. 126, The Harlow-Shapley Symposium on Globular Cluster Systems in Galaxies. p. 603

van der Wel A., et al., 2014, *ApJ*, **788**, 28

## APPENDIX A: COMPARISON OF MOCK SAMPLE TO SDSS

As an additional check to ensure that our mock sample of galaxies have reasonable properties, we plot the redshift and stellar mass number densities of our mock sample and the real data from the NASA Sloan Atlas catalog of  $z < 0.055$  SDSS galaxies, based on the SDSS data release 8 (Blanton et al. 2011) with  $\Omega \approx 9380 \text{ deg}^2$ . To ensure the comparison is consistent, we apply magnitude limits of  $r \approx 17.8$  mag to each sample using the spectroscopic targeting limit of SDSS after applying the rough filter conversions from Lupton (2005)<sup>8</sup>. We also assume a measurement uncertainty of 0.3 dex in stellar mass for our mock sample (Reines & Volonteri 2015). The result is shown in Figure A1. As expected, the mock sample and real sample have qualitatively similar redshift and mass distributions.

## APPENDIX B: HOST GALAXY DILUTION PARAMETERS

We compute the host galaxy Petrosian  $g - r$  color index from the version 0.1.2 of the NASA Sloan Atlas catalog of  $z < 0.055$  SDSS galaxies, based on the SDSS data release 8 (Blanton et al. 2011). In order to sample realistic colors for our galaxies in our model, we incorporate the bi-modality of the galaxy color population (e.g., Bell et al. 2003; Baldry et al. 2004). Because we are interested in observed colors at low redshifts, we use the observed Petrosian magnitudes without K-corrections or dust-corrections using the PETROFLUX key. We model the color-mass diagram ( $g - r$  versus stellar mass) as a mixture of elliptical Gaussians, following a similar approach to Taylor et al. (2015). We used the BayesianGaussianMixture module

<sup>8</sup> <http://www.sdss3.org/dr8/algorithms/sdssUBVRITransform.php#Lupton2005>

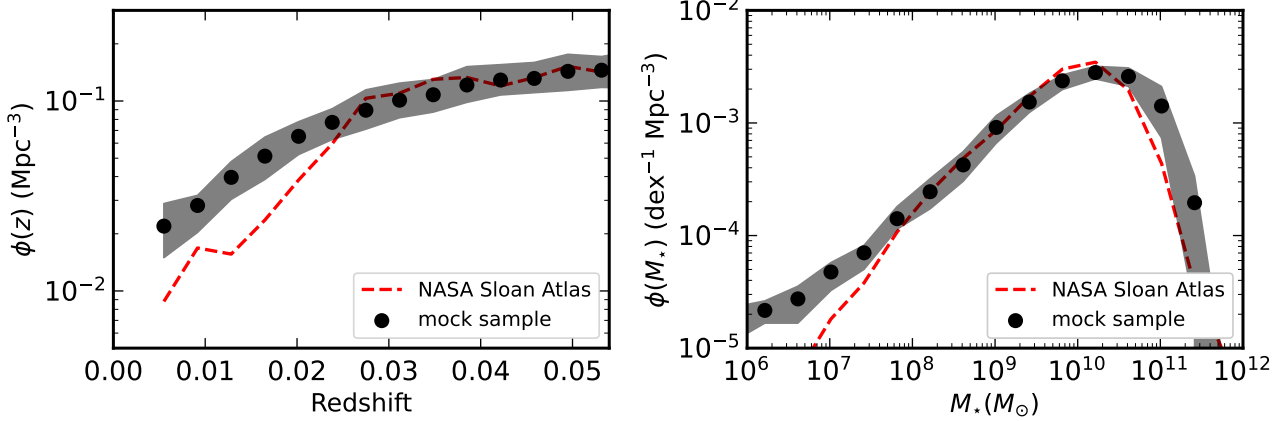


**Figure A1.** Distributions of galaxy redshifts (*left*) and stellar masses (*right*) for a mock sample with a limiting magnitude of  $r \approx 17.8$  (solid red line) and the NASA Sloan Atlas catalog of  $z < 0.055$  SDSS galaxies (dashed gray line). Our mock sample reproduces the observed distributions from the NASA Sloan Atlas reasonably well.

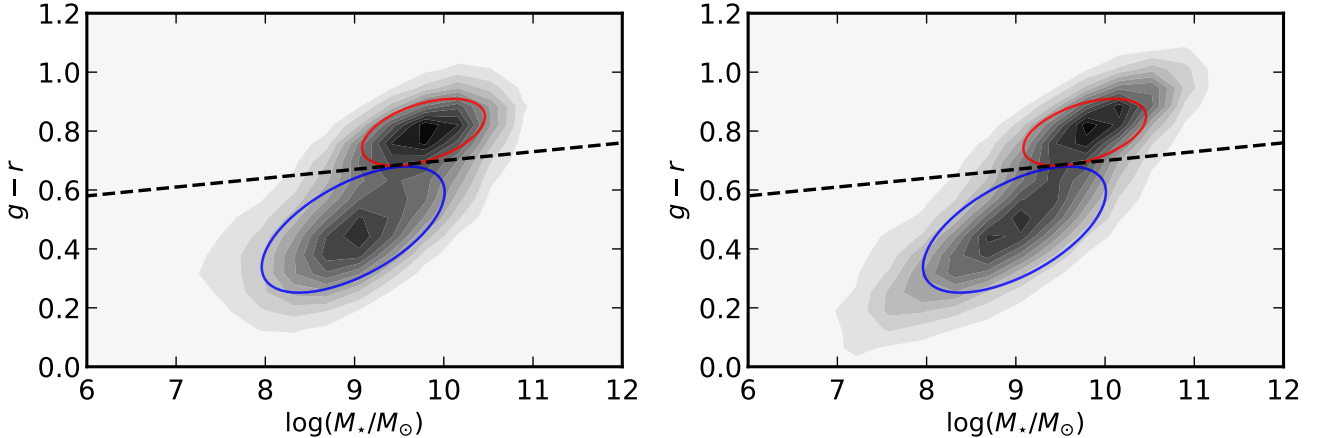


**Figure B1.** Host galaxy  $g - r$  color index versus stellar mass from the NASA Sloan Atlas catalog of  $z < 0.055$  SDSS galaxies (*left panel*) and for a mock sample with a limiting magnitude of  $r \approx 17.8$  (*right panel*). Darker contours represent denser regions of the distributions. The exact shapes of the contours depend on the limiting magnitude. The red and blue ellipses represent the  $1\sigma$  width of each distribution component our fitted Gaussian mixture model from the SDSS data, from which we randomly draw the galaxy colors for the red and blue populations in our Monte Carlo model. They are shown in both panels to facilitate comparison. The dashed black line shows the color-magnitude diagram slope of  $-0.03$  used to divide the red and blue galaxy populations (Bell et al. 2003).

implementation in `SCIKIT-LEARN` python package (Pedregosa et al. 2011). The  $g - r$  color indices are then sampled using these probability distribution functions at a given stellar mass for the red and blue galaxy populations separately using the respective GSMF (§2.1). The two Gaussian components representing the red and blue galaxy populations are shown on the color-mass diagram in Figure B1. A typical  $g - r$  color index value for a radiatively-efficient (blue) dwarf galaxy is  $g - r \approx 0.5$ .

We also compute the aperture contamination factor (covering factor) accounting for the level of host galaxy light dilution in a  $3''$  aperture, denoted  $f_{\star,3''}$ . We obtain these values by dividing the flux within a circular  $3''$  aperture by the total Petrosian flux as FIBERFLUX/PETROFLUX in the  $g$  band. There are two effects to consider. First, the aperture contamination increases with redshift as the typical galaxy angular size decreases. Second, the aperture contami-

nation increases as galaxy stellar mass decreases given the galaxy the size-mass relation (e.g., van der Wel et al. 2014). Therefore, we split the SDSS galaxies into bins of stellar mass and evaluate the  $f_{\star,3''} - z$  relations in each bin. We fit an empirical polynomial function of the form  $f(x) = 1 - 1/(x^2 + bx + c)$  where  $x \equiv z - a$ , which assures that  $f(x) \rightarrow 1$  as  $z \rightarrow \infty$ , to the distribution of  $f_{\star,3''}$  versus redshift  $z$ . The scatter in these relations is probably a function of the varying surface brightness profiles in the galaxy population. For example, galaxies with bright bulges will have larger  $f_{\star,3''}$  values. We adopt this simple best-fitting models and rms scatter in our Monte Carlo framework. The results for both are shown in Figure B2. A typical host galaxy dilution parameter value for dwarf galaxies near the median redshift of  $z \approx 0.03$  is  $f_{\star,3''} \approx 0.2$ .

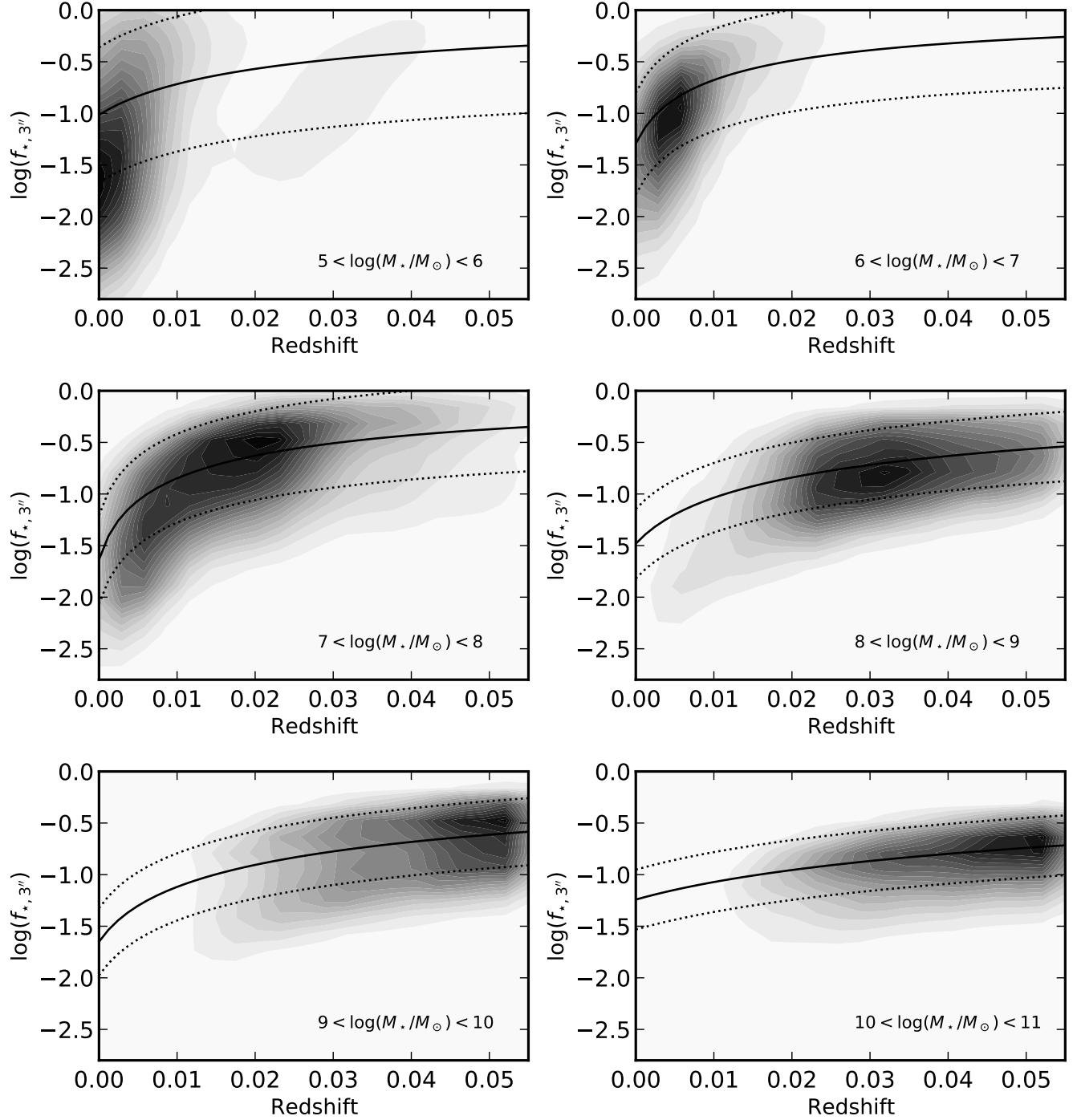


**Figure B2.** Host galaxy aperture contamination factor in a  $3''$ -diameter aperture  $f_{\star, 3''}$  versus redshift from the NASA Sloan Atlas catalog of  $z < 0.055$  SDSS galaxies in bins of stellar mass (marked on each panel). Darker contours represent denser regions of the distributions. Our adopted best-fitting model and rms scatter are shown as solid and dotted black lines, respectively.

### APPENDIX C: BLACK HOLE MASS DETECTION LIMITS

A light curve with detectable variability must have an rms variability amplitude greater than the photometric precision limit of the survey. For a sufficiently long light curve ( $t_{\text{baseline}} \gtrsim \tau$ ), the rms should approximate the asymptotic variability amplitude (host-

diluted)  $\text{SF}'_{\infty}$ . The detection limit is given by equating this with the photometric precision of the survey (Equations 13 and 14). Assuming the systematic component of the photometric precision is small (generally true at faint magnitudes), and ignoring the (small) first

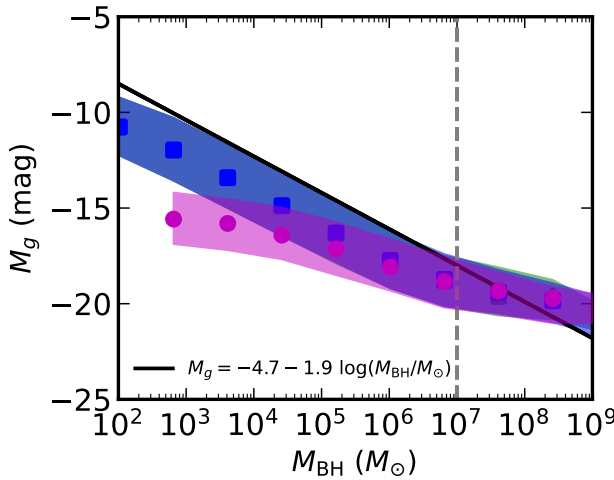


**Figure C1.** Combined host galaxy and AGN absolute magnitude - BH mass relation for our LSST Rubin (lower panel) -like models. The solid black line is a linear approximation of the 68th percentile to approximate the faint end of the population for use in computing the detection limits. The gray dashed lines represents the rough transition mass of  $M_{\text{BH}} \sim 10^7 M_{\odot}$ , below which the luminosity is significantly affected by the host galaxy light.

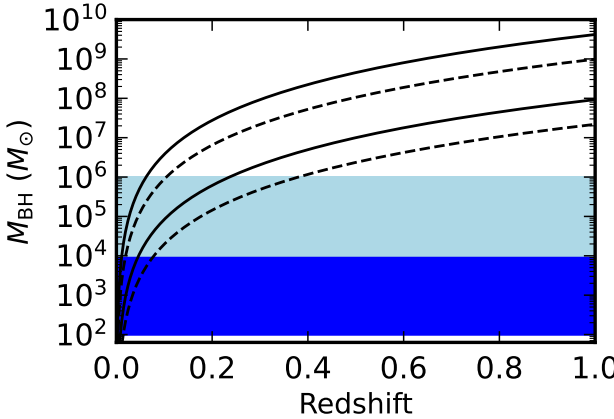


**Figure C2.** Theoretical BH mass detection limit for our PTF (upper pair of black curves) and LSST Rubin (lower pair of black curves) -like models assuming an rms variability amplitude of 0.1 (solid lines) and 0.3 mag (dashed lines). The light blue shaded area represents the range of “massive BHs” where the BHMFs begin to differ. The dark blue shaded area represents the IMBH regime.

order term of Equation 14 (i.e.,  $0.04 - \gamma \approx 0$ ), we have:

$$\text{SF}'_{\infty} \approx \gamma^{1/2} x. \quad (\text{C1})$$

Substituting  $x \equiv 10^{0.4(m-m_5)}$  above, we have:

$$\text{SF}'_{\infty} \approx \gamma^{1/2} 10^{0.4(m-m_5)}. \quad (\text{C2})$$

Taking  $m = M + 5 \log d_{\text{pc}} - 5 + K(z)$  where  $K(z)$  is the K-correction, and re-arranging:

$$2.5 \log(\text{SF}'_{\infty} \gamma^{-1/2}) \approx M + 5 \log d_{\text{pc}} - 5 + K(z) - m_5. \quad (\text{C3})$$

Here, the absolute magnitude  $M$  refers to the total magnitude of the host galaxy and the AGN. Noting that the BH mass and galaxy luminosity are correlated with some scatter determined by the scatter in both the mass-to-light ratios and host galaxy - BH mass relation, we assume the absolute magnitude can be described as by linear function of the form  $M = a + b \log(M_{\text{BH}}/M_{\odot})$  for small BH masses where the host galaxy light dominates, as shown in Figure C1. In the  $g$ -band, we find  $a = -4.7$  and slope  $b = -1.9$ . In  $R$ , an intercept of  $a = -6.0$  is more appropriate. Substituting above and solving for  $\log(M_{\text{BH}}/M_{\odot})$ , we have:

$$\log\left(\frac{M_{\text{BH}}}{M_{\odot}}\right) \approx \frac{1}{b} \left[ 2.5 \log(\text{SF}'_{\infty} \gamma^{-1/2}) - a - 5 \log d_{\text{pc}} + 5 - K(z) + m_5 \right]. \quad (\text{C4})$$

We show the BH mass detection limits for our PTF and LSST Rubin -like models in Figure C2, taking  $\text{SF}'_{\infty} = 0.1$  and  $\text{SF}'_{\infty} = 0.3$  mag (Figure 4). There is likely to be a complex mass dependence on the intrinsic variability amplitude, depending on the intrinsic BH mass dependence on the variability amplitude and the host galaxy luminosity (see §2.7), so we adopt these two scenarios as a simplification. The K-correction is assumed to be zero, because it is usually small for blue, star-forming dwarf galaxies (Chilingarian et al. 2010). The corresponding theoretical stellar mass detection limit can then be computed using the BH - host galaxy stellar mass relation.

#### APPENDIX D: VARIABLE FRACTION FOR THE RED AND BLUE HOST GALAXY POPULATIONS

Following §4.2, we show versions of Figure 11 for the blue and red host galaxy populations with different ERDFs (Weigel et al. 2017) with a 0.3 dex uncertainty on the stellar mass measurements. The results are shown in Figure D1 for our PTF and LSST Rubin -like models. Red host galaxies make up a larger fraction of the total variable AGNs with  $M_{\star} \gtrsim 10^{9.5} M_{\odot}$  while blue host galaxies dominate the variable dwarf AGNs with  $M_{\star} \lesssim 10^{9.5} M_{\odot}$ .

#### APPENDIX E: VARIABLE FRACTION FOR VARYING UNCERTAINTY ON STELLAR MASS MEASUREMENTS

Following §4.2, we show versions of Figure 11, which assumed a 0.3 dex uncertainty on the stellar mass measurements, with 0.6 dex and 0.9 dex uncertainties on the stellar mass measurements for comparison. The results are shown in Figure E1 for our LSST Rubin -like models. The stellar mass uncertainties have no effect on the variable fraction as a function of magnitude.

This paper has been typeset from a  $\text{TeX}/\text{L}\text{AT}\text{E}\text{X}$  file prepared by the author.

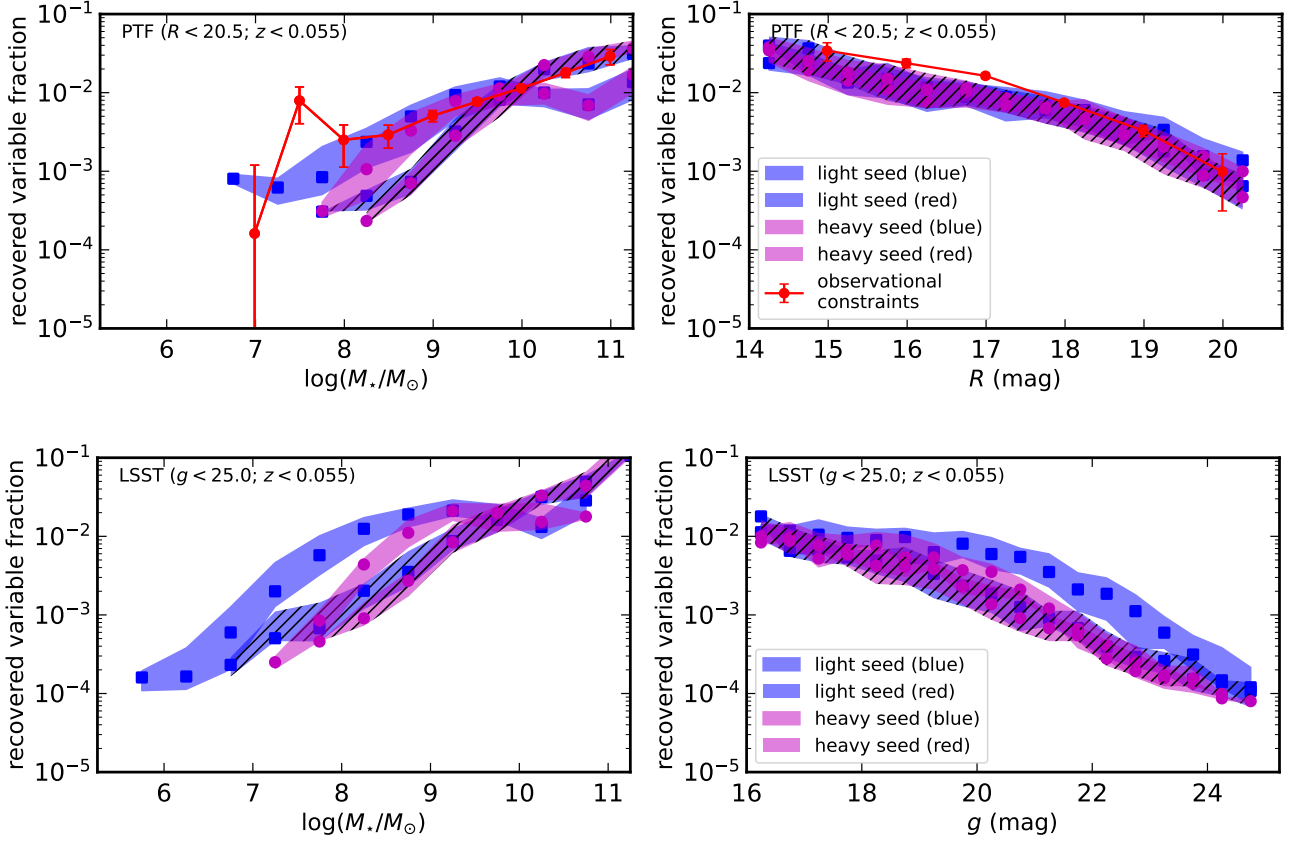


**Figure D1.** Same as the lower panel of Figure 11 but with the variable fractions computed separately for the blue (no hatching) and red (black hatching) host galaxy populations as a fraction of the total host galaxy population.

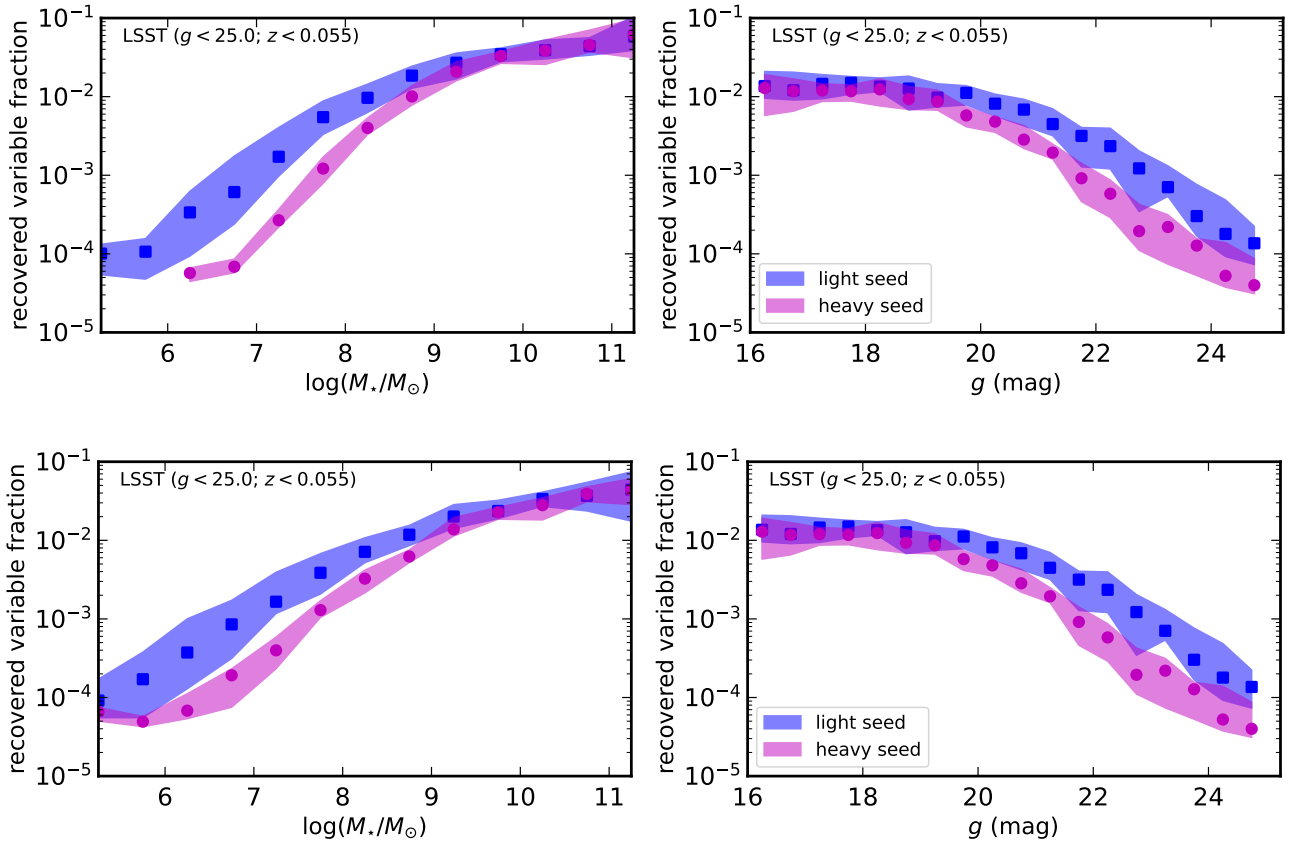


**Figure E1.** Same as the lower panel of Figure 11 but with 0.6 dex (upper panel) and 0.9 dex (lower panel) uncertainties on the stellar mass measurements.